Engineering Structures 292 (2023) 116494

Contents lists available at ScienceDirect

Engineering Structures

journal homepage: www.elsevier.com/locate/engstruct

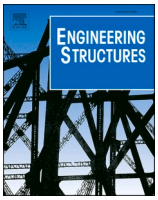

Modelling of laminated glass PVB walls of buildings exposed to vehicle impact with different speeds

Karol Grębowski *, Monika Zielińska

Gdansk University of Technology, Faculty of Architecture, Department of Technical Bases of Architectural Design, Faculty of Civil and Environmental Engineering, Department of Mechanics of Materials and Structures, Narutowicza 11/12, 80-233 Gdańsk, Poland

ARTICLE INFO

Keywords:
Glass-ply cracking
PVB laminated glass
Extrinsic cohesive model
Passive protection system
Laminated glass model
Crash tests
Mooney–Rivlin model

ABSTRACT

This paper presents an analytical model, developed for laminated glass subjected to a low-velocity impact. It has the ability to capture glass cracks as well as large non-linear deformations. It is based mathematically on the first-order deformation concept, which considers the effect of membrane and transverse shear as well as bending. This theory uses damage mechanics to capture the glass cracking. For this purpose, several experiments have been carried out based on PVB laminated glass. The history of acceleration, transverse central displacement and velocity estimated over time is in a favourable relationship with the experimental information. In terms of laminated glass, non-dimensional coefficients have been suggested that regulate both the first peak contact force and the maximum transverse displacement. Laminated glass consists of several layers of soda-lime glass sheets bound together by intermediate layers of polyvinyl butyral (or PVB). Cracking of the glass layer is the main cause of laminated glass damage under both low and high-speed impacts. The main objective of the present article is to conduct experimental studies and numerical analyses of the glass ply cracking mechanism as part of the development of new strength parameters for PVB laminated glass. The non-linear characteristics of PVB are described using the Mooney-Rivlin constitutive model. The present article proves that it is possible to precisely model a wall made of VSG (Verbund Sicherheits Glas) laminated glass reinforced with a vinyl interlayer of appropriate thickness, and further, that such walls can constitute an element absorbing the impact energy of vehicles with specific parameters such as a passenger car, buses, and HGVs (Heavy Goods Vehicle). Based on the results of our study, new parameters were elaborated to determine the properties of PVB laminated glass exposed to vehicle impact. These new parameters were verified qualitatively by comparing the simulation results with experimental observations. We also assessed the strength of a wall of adequate thickness made of laminated glass at the ground floor level of a building exposed to a high-risk terrorist attack. The developed analytical model allows for a quick and reliable assessment during the initial design of safety glass, where a full-scale FE analysis is often too time-consuming.

1. Introduction

The current state of knowledge of the protection and safety of people and buildings exposed to terrorist threats is currently being overlooked in the standards for designing public buildings and infrastructure. Analysis of the available data proves that terrorist at-tacks cannot be fully prevented. However, their effects can be minimized by appropriately designing passive protection system elements, by creating walls made of laminated glass.

Our analysis of the subject literature revealed that currently there are no guidelines and procedures that would allow for the design of structural glass elements working as walls. Of all the currently used construction materials, such as: concrete, steel, wood, glass strength, as well as its behaviour under load conditions, it is the least researched. One of the attempts to organize knowledge about the properties and mechanical performance of glass was the preparation and development of the European Standard EN 572, Glass in building (2004). Nevertheless, a more detailed analysis of the said document reveals that it mainly concerns glass elements working as slabs in the facades of buildings, which are stressed only with their own weight and wind loads. Structural elements of glass are destroyed rapidly and do not demonstrate any plastic deformation, which is why glass is the most difficult and unpredictable structural.

* Corresponding author.
E-mail addresses: karol.grebowski@pg.edu.pl (K. Grębowski), monika.zielinska@pg.edu.pl (M. Zielińska).

https://doi.org/10.1016/j.engstruct.2023.116494
Received 17 February 2023; Received in revised form 15 May 2023; Accepted 13 June 2023
Available online 30 June 2023

Laminated glass is a simple composite structure with wide applications in construction. It is considered to be a safe glass because it has a good energy absorption capacity and, in case of breakage, most of the glass fragments remain bound by the intermediate layer of PVB. This significantly reduces the risk of injury caused by projected glass shards.

Soda-lime glass is the brittle component of laminated glass. The film, on the other hand, is a hyperelastic rubber-like material. Glass and film are bonded by an adhesive bond, which is influenced by many factors such as the washing process during production or the moisture content of the vinyl interlayer. In practice, glass and the vinyl inter-layer are not fully interconnected. High adhesion laminated glass promotes the bonding of fragments of cracking glass, which in turn results in its low resilience [1,2]. In the production process of laminated glass, the relationship between resilience and adhesion is optimized. The combined properties of glass brittleness, non-linearity of the vinyl inter-layer, and adhesive bonding make the mechanism of cracking of laminated glass as a result of impact damage far more complicated than in the case of monolithic glass.

In recent years, there were tests of the mechanical properties of laminated glass carried out using theoretical analyses [2–8], experimental methods [2,9–15], as well as numerical simulations [2,10,18–43]. First of all, Xu [14–17] experimentally investigated the be-haviour of glass layer cracking in a laminated glass panel. Response of cracked laminated glass have been described by Galuppi [44], Muralidhar [45], Biolzi [41] and Galuppi [46]. Numerical models for both undamaged and broken laminated glass have been described by Ivanov [47], Baraldi [48] and Freddi [49]. The polymers' viscoelasticity strongly influences the laminated glass response [50–52], in particular under blast loadings [53]. Also the stiffness of the rear structure strongly influences the response of laminated glass plates under blast and impact loads [54–66]. In the case of numerical simulations, modelling of cracking of glass layers was carried out using the element deletion method available in the LS-DYNA [10] and ABAQUS software suites [19–24], as well as the damage continuum method [27,28], the combined DE discrete elements and FE finite elements method [29–32] and the XFEM extended finite element method [33]. Chen [34] simulated the propagation of cracks in laminated glass under the impact of dynamic load in the form of a weight impact, in which they applied an external cohesion model [2]. The phenomenon of anisotropy, in which the mechanical properties of the material are different in different directions, also plays a very significant role in laminated glass. Generally speaking, the mechanical properties of anisotropic materials are not symmetrical with respect to any of their planes or axes. Voyiadjis [67] developed the gradient damage theory for anisotropic damage for impact problems. In addition Voyiadjis [67] extended the gradient theories to rate-dependent plasticity or damage. Lu [68] presented the role of covariant constitutive description of anisotropic non-linear elasticity in which the necessary conditions for covariance of anisotropic strain energy functions and alternative representations of the stress response were derived. Additionally, Sumelka [69] presented the plate anisotropy induced by plastic strain evolution and rate-dependence influenced by impact loads. Safaei [70] presented an evolutionary anisotropic model for sheet metals based on the non-associated flow rule whereby they proposed a phenomenological approach to describe the evolution of anisotropy in the uniaxial deformation path using sets of parameters associated with various equivalent plastic strain levels. A numerical implementation of an anisotropic constitutive model is presented in Manzari [71]. The presented numerical simulations are compared with the field measurements. The drawbacks of using an isotropic elasto-plastic model are also demonstrated.

It should be kept in mind that applying different numerical methods for laminated glass results in the possibility of using different modelling techniques. Researchers usually use combinations of shell elements with membrane elements to model laminated glass [2,10,23,24]. The glass is discretized as shell elements, while the vinyl interlayer deformation is described using membrane elements. The connection between these elements is made using a contact algorithm or a shared node approach. Larcher [10] created a model of a laminated shell element for laminated glass with extended destruction criteria, as well as a model using brick elements. They then compared the results of the analyses with the results of the fuzzy model proposed by Timmel [21]. In the case of the combined DE/FE method, the vinyl interlayer is discretized into brick finite elements, because it is sensitive to large deformations. However, one should be cognizant that all or at least some part of the glass in which the crack is to be formed must be discretized into discrete elements [29–32]. In these models, adhesion is modelled by combining discrete elements in glass with finite elements in the vinyl interlayer. Therefore, the algorithm of contact between the glass and the vinyl interlayer can be divided into two groups: the penalty-based models and the shared-node model. The penalty-based models are based on relative shifts be-tween glass and vinyl interlayer by imposing penalty forces. However, in the shared-node models, there are no relative shifts between the layers forming the laminated glass [2].

In the present article, we will focus on the experimental and numerical examination of the cracking of glass layers, because cracks and scratches constitute the main pattern of damage in laminated glass [24,27]. During the study of cracking prediction, an external cohesion model was applied, which is capable of eliminating the numerical problem of artificial susceptibility, which occurs in the intrinsic cohesive models [34]. In addition, a model of laminated glass was proposed, in which brick elements and an intrinsic cohesive formulation were applied. The brick elements were selected instead of the shell elements because during the research we focused on modelling the crack propagation de-pending on the thickness of the glass. The subject literature proves that the properties of PVB vinyl interlayer affect the mechanical properties of laminated glass subjected to a load in form of an explosion or impact with a vehicle [2,26,35]. In designing such structures, one needs to remember that the destruction of glass occurs momentarily with no plastic deformation. What follows is glass is recognized as one of the most difficult and unpredictable construction materials to work with. That is why the new technical specifications CEN / TS 19100: 2021 "Design of glass structures" were created in 2021. CEN / TS 19100 is intended to pave the way for Eurocode of Structural Glass in the transition period [57].

The research carried out in the present article and the results obtained are innovative. Based on experimental and numerical research, new parameters were developed to determine the properties of laminated glass consisting of VSG laminated glass reinforced with PVB interlayers exposed to vehicle impact. We also assessed the strength of the laminated glass wall (taking into account the new material parameters) with an appropriate thickness at ground floor level in a building with a high degree of terrorist threat in terms of vehicle impact.

2. Methodology

2.1. Laminated glass model

In the present work, in order to simulate the cracking of the glass layer, a three-dimensional modified Camacho-Ortiz model was applied, taking into account behaviours that depend on the path [34]. The cracking condition of the cohesive model is based on stress, which is equivalent to the fact that the cohesive element is placed adaptively on a common surface between two elements, when the acting traction force T_e is greater than the cohesive strength σ_{max}:

$$T_e \geq \sigma_{max} \tag{1}$$

The task of this model is to implement an independent parameter κ to specify the ratio that occurs between the normal crack energy ψ_t and the tangential crack energy ψ_n, resulting in the dissipation of the crack energy, which depends on the following path:

$$\kappa = \frac{\psi_t}{\psi_n} \tag{2}$$

The effective opening displacement Δ_{eff} can be defined as:

$$\Delta_{eff} = \sqrt{\frac{\eta^2}{\kappa^2}\Delta_t^2 + \langle \Delta_n \rangle^2} \tag{3}$$

then the $\Delta_t = \sqrt{\Delta_{t1}^2 + \Delta_{t2}^2}$; Δ_n is the component of normal displacement, and Δ_{t1}^2 & Δ_{t2}^2 determines the tangential components of the displacement; whereas η is used in the case of the Camacho-Ortiz model to present the result of the mixed mode; and the operator $\langle \bullet \rangle$ is expressed as follows:

$$\langle x \rangle = \begin{cases} x, x \geq 0 \\ 0, x < 0 \end{cases} \tag{4}$$

A coherent traction force vector $\boldsymbol{T}$ is then determined using the following formula:

$$\boldsymbol{T} = \frac{\sigma_{max}}{\Delta_{eff(\max)}}\left(1 - \frac{\Delta_{eff}}{\delta_c}\right)\left(\frac{\eta^2}{\kappa^2}\Delta_t + \Delta_n \boldsymbol{n}\right) \tag{5}$$

where $\Delta_{eff(\max)}$ denotes the maximum displacement in history; σ_{max} expresses cohesion strength; δ_c represents the critical displacement of the opening; $\boldsymbol{n}$ is a normal unit outside; $\Delta_t = \Delta + \Delta_n \boldsymbol{n}$, and Δ defines the displacement vector.

Therefore, it is possible for the tangent and normal resultant cohesive force, T_n and T_t to be determined using the following method:

$$T_n = \sigma_{max}\left(1 - \frac{\Delta_{eff}}{\delta_c}\right)\frac{\Delta_n}{\Delta_{eff(\max)}} T_t = \frac{\eta^2}{\kappa^2}\sigma_{max}\left(1 - \frac{\Delta_{eff}}{\delta_c}\right)\frac{\Delta_t}{\Delta_{eff(\max)}} \tag{6}$$

Two aspects should be considered in order to correctly model the finite elements for laminated glass. First, we need to correctly select the type of element, and secondly, we need to correctly perform the adhesion model. Shell elements are popular in glass modelling because they have a small number of elements, which in turn affects the possibility of using less computing power. However, such a solution renders it impossible to examine the impact of cracking depending on the thickness of the glass [2,10,23,24]. Therefore, in order to check the cracking mechanism during the tests, taking into account the thickness of the glass, brick elements are used, which additionally allowed for more accurate results. Such elements were also adopted in the present work [2,18–21]. However, it should be borne in mind that the use of brick elements may cause serious deviations in the mesh. Such a situation can be remedied by the use of the adaptive remeshing method [37].

In relation to the modelling of the connection between glass and vinyl interlayer, two types of numerical algorithms can be found in the subject literature, i.e., the penalty-based approaches and the shared-node algorithm [24,29]. However, in the present work, we adopted an intrinsic cohesive formulation, as an alternative thereto [35]. Fig. 1 presents a two-dimensional beam of laminated glass during its destruction. In this figure, it can be seen that under the influence of transverse load, the crack in the outer glass propagates from the border between the outer glass and the vinyl interlayer [2,12]. It should be noted that the use of the shared-node algorithm does not allow for an accurate representation of the imperfect adhesion between the glass and the vinyl interlayer. As the crack propagates in the top layer of glass it can be reduced during the load increment (Fig. 1a). When it comes to the penalty-based algorithm, adhesion strength can be adjusted by changing the value of the penalty stiffness [2].

In the work from the intrinsic cohesive models, an improved Xu-Needleman model [61] was applied to model the adhesion between the layer of glass and the vinyl interlayer, as accurately as possible. In this model, the normal cohesive forces T_n and the tangential cohesive forces T_t can be calculated as follows:

$$T_n = \frac{\psi_n}{\delta_n}\left(\frac{\Delta_n}{\delta_n}\right) exp\left(-\frac{\Delta_{n(max)}}{\delta_n}\right) exp - \frac{\Delta_{t(max)}^2}{\delta_t^2} T_t = 2\frac{\psi_t}{\delta_t}\left(\frac{\Delta_t}{\delta_t}\right)\left(1 + \frac{\Delta_{n(max)}}{\delta_n}\right) exp\left(-\frac{\Delta_{n(max)}}{\delta_n}\right) exp - \frac{\Delta_{t(max)}^2}{\delta_t^2} \text{ Where } \frac{\psi_n}{\sigma_{n(max)} exp(1)} \text{ and } \delta_t = \frac{\psi_t}{\sigma_{t(max)}\sqrt{\frac{1}{2}exp(1)}} \tag{7}$$

where ψ_n – the normal fracture energy, ψ_t – the tangential fracture energy, $\sigma_{n(\max)}$ – the normal cohesive strength, $\sigma_{t(\max)}$ – the tangential

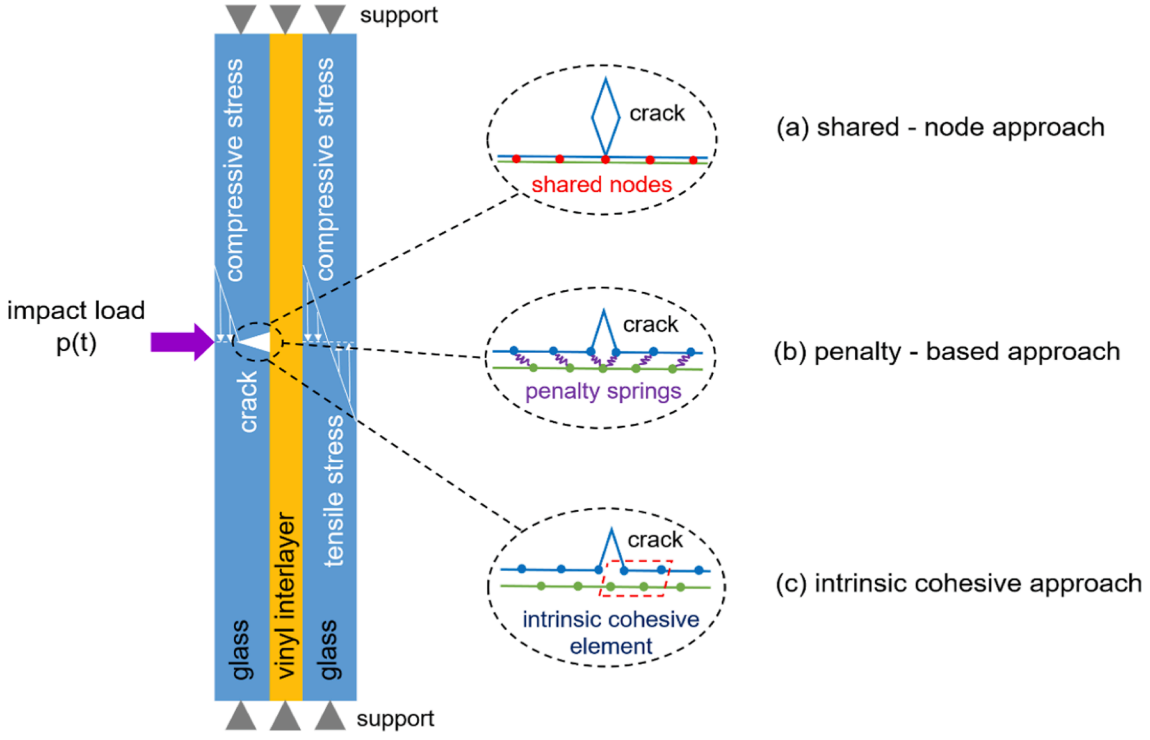

Fig. 1. Three kinds of numerical approaches for the modelling of the adhesion between glass and PVB [2].

cohesive strength, δ_n – the normal critical opening displacement, δ_t – the tangential critical opening displacement, Δ_n – the normal displacement components and Δ_t – the tangential displacement components.

Parameters $\Delta_{n(max)}$ and $\Delta_{t(max)}$ correspond to the maximum stretching and shear displacements over time. On the other hand, $\sigma_{n(max)}$ and $\sigma_{t(max)}$ are the maximum normal and tangential stresses in pure tensile and shear traction-separation curves.

2.2. Contact algorithm

The article applies an efficient global and brick local contact algorithm for the simulation of cracks, as developed by Chen et al. [34]. When it comes to the global contact algorithm, it includes both regular and adaptive search. Regular searching is carried out by using a linear contact algorithm called LC-GriD [39]. During the propagation of external cracks, new bonds are created adaptively through adaptive insertions of cohesive elements. Therefore, an adaptive search algorithm was applied to effectively and continuously update newly formed contacts. The local contact algorithm generates node-surface and edge-edge contacts [2,40].

After the crack penetration occurs in the local contact algorithm, the contact is automatically forced to counteract the penetration. Normal contact force f_n is determined with the use of the penalty function method:

$$\boldsymbol{f}_n = k \bullet g \cdot \boldsymbol{n}_s \tag{8}$$

where g is the penetration depth. Furthermore $\boldsymbol{n}_s$ denotes the unit normal vector, and k is the stiffness coefficient.

The Coulomb model was applied to calculate the frictional force:

$$\boldsymbol{f}_t = -\mu \bullet \boldsymbol{f}_n \bullet \boldsymbol{n}_t \tag{9}$$

where $\boldsymbol{f}_n$ is the magnitude of the normal force. The variable μ is the Coulomb friction coefficient, and $\boldsymbol{n}_t$ denotes the unit tangent vector [2].

2.3. The constitutive model of vinyl interlayer

The non-linear characteristics of the vinyl interlayer were described using the constitutive Mooney-Rivlin model [21].

The deformation gradient $\boldsymbol{F}$ can be adopted as:

$$\boldsymbol{F} = 1 + \frac{\partial \boldsymbol{u}}{\partial \boldsymbol{X}} \tag{10}$$

where 1 is the identity tensor. On the other hand, $\boldsymbol{u}$ is the displacement vector and $\boldsymbol{X}$ the reference position vector.

Due to the fact that the vinyl interlayer is a virtually incompressible hyperelastic material,

to be able to use low-order elements, the F-bar method is applied for its analysis [41]. This method releases volumetric locking. The modified deformation gradient $\widetilde{\boldsymbol{F}}$ is then defined to alleviate the limitations of non-compressibility:

$$\widetilde{\boldsymbol{F}} = \left[\frac{det(\boldsymbol{F}_0)}{det(\boldsymbol{F})}\right]^{\frac{1}{3}} \boldsymbol{F} \tag{11}$$

where $\boldsymbol{F}_0$ is the current deformation gradient located at the centre of gravity of the element. The above definition enables us to counteract volumetric blocking because it indicates that the $\widetilde{\boldsymbol{F}}$ determinant is constant for the element and is equal to the determinant of the deformation gradient in the middle of the element, i.e.,$det\left(\widetilde{\boldsymbol{F}}\right) = det(\boldsymbol{F}_0)$.

The Cauchy-Green strain relief tensor $\boldsymbol{C}$ is defined by the following formula:$\boldsymbol{C} = \widetilde{\boldsymbol{F}}^t \widetilde{\boldsymbol{F}}$.

The Mooney-Rivlin model is applied, and the corresponding deformation energy function is described by input constants A and B [42]:

$$W(I_1, I_2, I_3) = A(I_1 - 3) + B(I_2 - 3) + D\left(\frac{1}{I_3^2} - 1\right) + E(I_3 - 1)^2 \tag{12}$$

where $I_1 = tr(\boldsymbol{C}), I_2 = \left[I_1^2 - tr\left(\boldsymbol{C}^2\right)\right]/2$ & $I_3 - det(\boldsymbol{C})$ are the invariants of deformation; forcing the reduction of non-compressibility. Whereas the constants D & E can be defined as:

$$D = \frac{1}{2}A + B \text{and} E = \frac{A(5\nu - 2) + B(11\nu - 5)}{2(1 - 2\nu)} \tag{13}$$

where ν is Poisson's ratio. It should be noted that if we differentiate the function of deformation energy in relation to the proper Cauchy-Green deformation tensor $\boldsymbol{C}$ the second Piola-Kirchhoff stress tensor $\boldsymbol{S}$ will adopt the form of:

$$\boldsymbol{S} = 2\frac{\partial W}{\partial \boldsymbol{C}} = 2\frac{\partial W}{\partial I_1}1 + 2\frac{\partial W}{\partial I_2}(I_1 1 - \boldsymbol{C}) + 2\frac{\partial W}{\partial I_3} I_3 \boldsymbol{C}^{-1} \tag{14}$$

The Cauchy stress tensor $\boldsymbol{T}_c$ is coupled to the second Piola-Kirchhoff stress tensor $\boldsymbol{S}$ by:

$$\boldsymbol{T}_c = \frac{1}{J}\widetilde{\boldsymbol{F}}\boldsymbol{S}\widetilde{\boldsymbol{F}}^T \text{ where } J = det\left(\widetilde{\boldsymbol{F}}\right) \text{is the relative volume [2].} \tag{15}$$

2.4. New generalised damage model of vinyl interlayer

Damage was included in the model of vinyl interlayer using a new generalised damage model: MAGD. MAGD was implemented to add anisotropic damage to already existing material models. Therefore, standard LS-DYNA materials (*MAT_…) can now be supplemented by a new keyword *MAT_ADD_GENERALIZED_DAMAGE. This enables an arbitrary definition of the damage tensor, a wide selection of several history variables, different possibilities to define a damage strain coordinate system and separate treatment of damage evolution for each history variable. Damage is often non-isotropic due to microcracking more or less perpendicular to the largest positive principal stress. Another cause is associated to the very anisotropic nature of the material which leads to stronger or weaker directions when it comes to softening and failure. In order to account for this kind of "anisotropic damage" we suggest introducing fourth order damage-effect tensor **M**:

$$\boldsymbol{\sigma} = \boldsymbol{M}^{-1} : \widetilde{\boldsymbol{\sigma}} \tag{16}$$

Many different concepts exist for the definition of that tensor, but in general it should have a structure (i.e., arrangement of zero and non-zero entries) similar to common constitutive tensors relating stress and strain tensors. The general framework of MAGD offers a good deal of flexibility in defining this damage tensor or better "damage matrix" since Voigt notation will be used. The fourth-order damage-effect tensor $\boldsymbol{M}^{-1}$ of equation (16) becomes a 6x6 matrix in Voigt notation and will be renamed $\boldsymbol{D}$ here. With the assumption of orthotropy (two orthogonal planes of material property symmetry), it contains up to 12 non-zero components D_{ij} to describe the relation between nominal (damaged) stresses σ_{ij} and effective (undamaged) stresses $\widetilde{\sigma}_{ij}$:

$$\begin{bmatrix} \sigma_{11} \\ \sigma_{22} \\ \sigma_{33} \\ \sigma_{12} \\ \sigma_{23} \\ \sigma_{31} \end{bmatrix} = \begin{bmatrix} D_{11} & D_{12} & D_{13} & 0 & 0 & 0 \\ D_{21} & D_{22} & D_{23} & 0 & 0 & 0 \\ D_{31} & D_{32} & D_{33} & 0 & 0 & 0 \\ 0 & 0 & 0 & D_{44} & 0 & 0 \\ 0 & 0 & 0 & 0 & D_{55} & 0 \\ 0 & 0 & 0 & 0 & 0 & D_{66} \end{bmatrix} \begin{bmatrix} \widetilde{\sigma}_{11} \\ \widetilde{\sigma}_{22} \\ \widetilde{\sigma}_{33} \\ \widetilde{\sigma}_{12} \\ \widetilde{\sigma}_{23} \\ \widetilde{\sigma}_{31} \end{bmatrix} \tag{17}$$

Now, each of the damage tensor components D_{ij} is a function of up to three damage variables D_1, D_2, and D_3:

$$D_{ij} = f(D_1, D_2, D_3) \tag{18}$$

An assumption is used in MAGD based on the effective plastic strain rate $\dot{\varepsilon}^{p}_{eff}$ (which is available for all plasticity based models) and the total strain rate tensor $\dot{\boldsymbol{\varepsilon}}$ (also always available) to obtain the plastic strain rate tensor $\dot{\boldsymbol{\varepsilon}}^{p}$:

$$\dot{\boldsymbol{\varepsilon}}^{p} = \frac{\dot{\varepsilon}^{p}_{eff}}{\dot{\varepsilon}_{eff}}\left[\dot{\boldsymbol{\varepsilon}} - \frac{\dot{\varepsilon}_{vol}}{3}\boldsymbol{\delta}\right] \tag{19}$$

After the selection of the damage tensor setup and the definition of history variables, the evolution laws for the damage variables have to be specified. The idea of MAGD is that each of the NHIS damage variables can be defined independently using the GISSMO parameters and equations. This means that, for each damage variable, the following evolution law applies:

$$\dot{D}_n = DMGEXP_n \bullet D_n^{\left(1-\frac{1}{DMGEXP_n}\right)} \bullet \frac{\dot{HIS}_n}{\varepsilon_{f,n}} \tag{20}$$

where $\dot{HIS}_n$ is the time derivative of the history variable, $\varepsilon_{f,n}$ is the "failure strain", and $DMGEXP_n$ is an input parameter. In GISSMO, a nonlinear stress coupling term is used incorporating a critical damage value $DCRIT_n$ and a fading exponent $FADEXP_n$. The same approach is adopted here for each damage variable separately, i.e., the damage variable is internally replaced by this expression:

$$D_n \rightarrow \left(\frac{D_n - DCRIT_n}{1 - DCRIT_n}\right)^{FADEXP_n} \tag{21}$$

3. Validation of the parameters of VSG laminated glass with PVB interlayer

3.1. Experimental setup

Validation of the VSG glass and vinyl interlayer parameters was carried out on the basis of both experiments and numerical analyses. For the tests, we used laminated glass panels, which were then subjected to a low-velocity dynamic impact load.

The experimental setup consisted of a square steel frame to which individual samples of glass panels were attached. In order to obtain constant boundary conditions, the samples were clamped around their circumference using 24 bolts (6 bolts on each side). The geometrical model is presented in Fig. 2.

The panels were in the shape of a square measuring 1000 × 1000 mm. For the experiments, a 2.28 mm thick PVB interlayer was used. It was also reinforced at the production stage. The thickness of a single interlayer is composed of six individual 0.38 mm thick films bonded with each other (6x0.38 mm = 2.28 mm), so that it has a greater strength. The glass panel was made of VSG tempered glass instead, which is why its strength was greater than the strength of a float glass panel. The low-velocity impact was achieved using a steel sphere. The sphere had a radius of 85 mm and a weight of 4.96 kg. We used the BiA500 launcher to launch the sphere in the direction of the sample,

Table 1
Thickness of the respective layers of laminated glass panels.

Test no.	Interlayer material	Thickness (mm) $h_{glass} + h_{PVB} + \ldots + h_{PVB} + h_{glass}$	Impact velocity (m/s)
1	PVB	20 + 2.28 + 20 + 2.28 + 20	10.00

allowing the sphere to reach an impact speed of 10 m/s at the centre of the panel. The speed value was read using a pair of laser speed meters. Experimental and numerical tests were carried out for a total of 20 samples with individual layer thicknesses adopted in accordance with Table 1.

NAC MemreCam GX-5 high-speed cameras were used to record the course of the tests. Three-dimensional sensors were also installed to measure displacement, velocity, and acceleration over time. During the experimental research, measurements of stresses, deformations, displacements, degradation at compression, and tensile and impact force were also carried out.

After conducting the tests in the laboratory, numerical tests were carried out for an identical experimental set.

3.2. Numerical simulation

Numerical simulations were performed using the LS-DYNA suite, which is an advanced tool used to analyze fast-changing phenomena as a function of time. Numerical calculations were performed using the Explicite procedure. The FE model was formed of 8 nodal cubic elements of reduced integration with a linear function of the C3D8R shape. We select brick elements instead of shell elements for glass in order to model the crack propagations through the glass thickness. PVB film is discretized into brick finite elements because it is prone to large deformation. The advantages of brick elements over tetrahedral elements are primarily higher accuracy. The size of the FEM mesh was 1 mm in the ×, y, and z directions, respectively. The convergence criterion assumed for defining the best mesh discretization was adopted based on displacement at point. The grid size was considered correct when the difference in the displacement results, at the point between the two grid pitch sizes, was approx. 2%. In the sample all degrees of freedom at the boundaries are fixed. The numerical model contained 1 686 600 brick elements. The material MAT_32-LAMINATED_GLASS and MAT_112- FINITE_-ELASTIC_STRAIN_PLASTICITY had been assigned to the FE model. It was assumed that the sphere is of rigid material and the glass is nonlinearly elastic. The energy release rates of glass are 10 N/m for mode I and 50 N/m for modes II and III [33]. The PVB was modelled using the Mooney-Rivlin constitutive model, and the corresponding constants are A = 1.6 MPa and B = 0.06 MPa [21]. The parameters of the intrinsic cohesive model for the modelling of the adhesion are $\boldsymbol{\psi_n} = \boldsymbol{\psi_t} = 100N/\boldsymbol{m}$ and $\boldsymbol{\delta_n} = \boldsymbol{\delta_t} = 0.001\boldsymbol{mm}$ [43].

Strain-rate sensitivity (SRS) of flow stress is an important parameter for the deformation mechanism of materials. Strain rate sensitivity was taken into account in the Mooney-Rivlin model. The Mooney-Rivlin

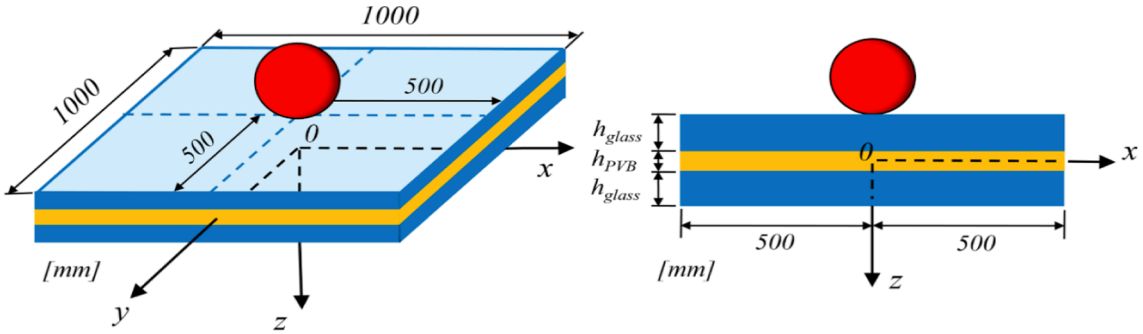

Fig. 2. Layout of laminated glass to impact of a rigid spherical projectile.

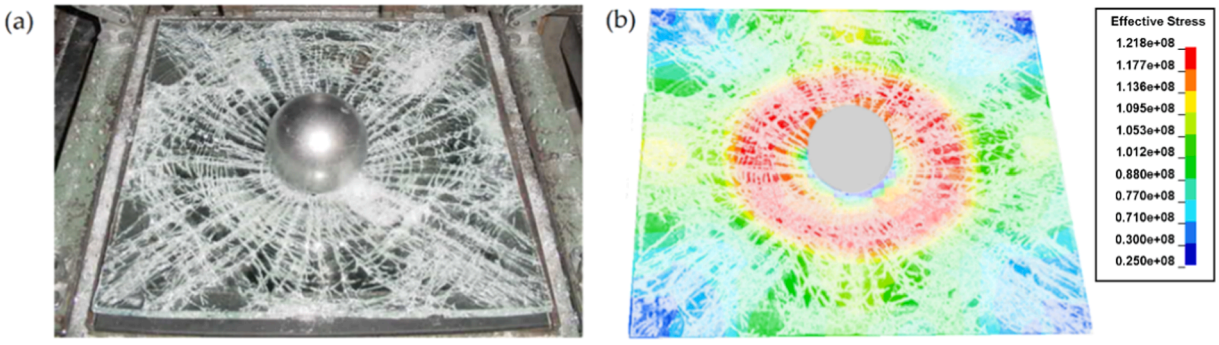

Fig. 3. Comparison of the results of (a) experimental setup and (b) numerical simulation for the sample with Test no. 1.

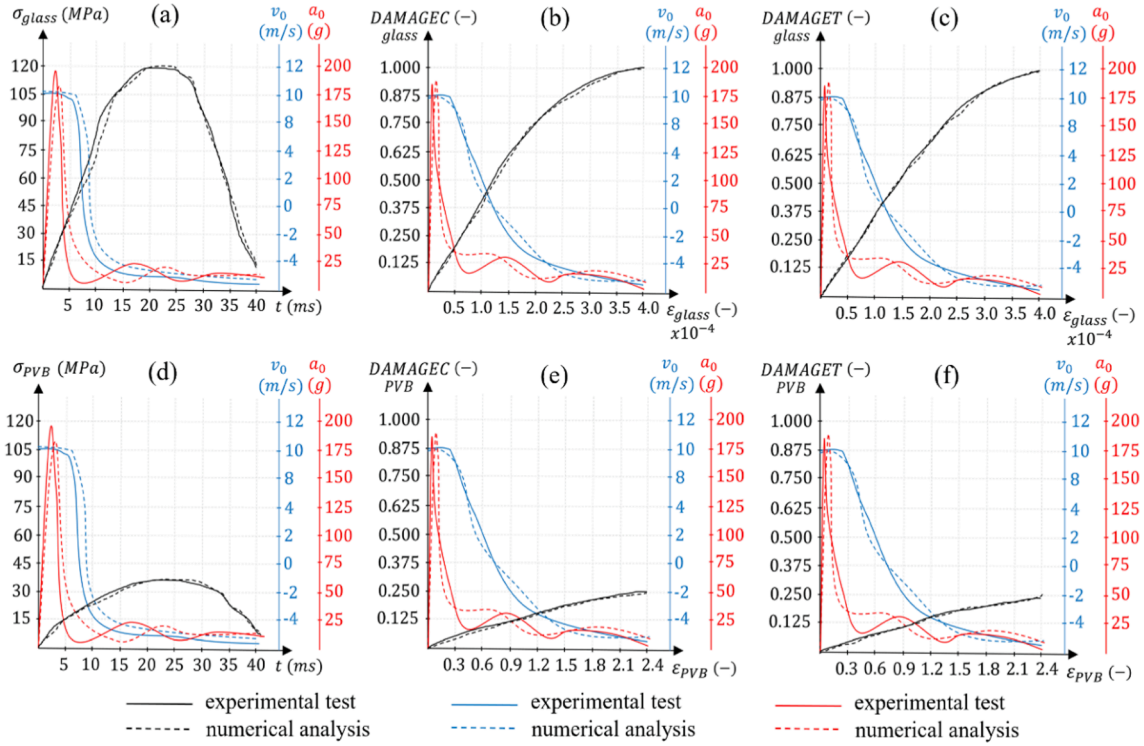

Fig. 4. Comparison of the results of experimental tests and numerical simulations based on the interpolation of the values of the results for 20 repetitions of sample destruction for Test no. 1.

model is able to correctly describe the behaviour of the PVB material in case of significant deformations and deformation speeds of from 100 to 5000 s^{-1}. The strain rates range from 100 to 5000 s^{-1} are able to cover the range of strain rates of PVB material in the impact damage process of laminated glass walls at the speeds of 120 km/h and below.

High computing power was required to perform these calculations. Therefore, the TRITON supercomputer available in CI TASK at the Gdansk University of Technology in Poland was used for numerical simulations. It is currently the fastest computer in Poland and the 12th fastest worldwide.

Based on the obtained results, strength parameters describing the material of VSG laminated glass reinforced with PVB film spacers were developed, including: mass density (RO), Young's modulus for glass (EG), Poisson's ratio for glass (PRG), yield stress for glass (SYG), plastic hardening for glass (ETG), plastic strain at failure for glass (EFG), Young's modulus for polymer (EP), Poisson's ratio for polymer (PRP), yield stress for polymer (SYP), plastic hardening for polymer (ETP), and plastic strain at failure for polymer (EFP).The results obtained during experimental and numerical research were compared and presented in Figs. 3 and 4.

3.3. Results

The prediction of damage to the laminated glass panel discovered during experimental research is analogous to the damage that occurred during numerical analyses. The resulting scratches and cracks of the glass coincide, with an accuracy of 1 mm.

In Fig. 4, we presented the results in the form of graphs elaborated on the basis of interpolation of the values of the results obtained during the 20 repetitions of the sample tests with Test no. 1.

We proved that it is possible to effectively and efficiently validate the parameters of the model of PVB interlayers reinforced VSG glass. The results acquired during experimental research and numerical calculations coincide at virtually every point in time, and the maximum difference between the resulting values is less than 3.2%. The maximum glass tension σ_{glass} amounted to approx. 120 MPa with a deformation

ε_{glass} of approx. 0.0004, for which the compression degradation variable *DAMAGEC* and the tensile degradation variable was 1.000. However, the maximum PVB stresses σ_{PVB} amounted to approx. 38 MPa with a deformation ε_{PVB} of approx. 2.4, for which the compression degradation variable *DAMAGEC* and the tensile degradation variable were 0.250.

On the basis of the obtained results of experimental research and numerical analyses, new parameters of laminated glass were developed, which may constitute an input.*m*at file for MAT_32-LAMINATED_GLASS and MAT_112FINITE_ELASTIC_STRAIN_PLASTICITY implemented in the material database in the LS-DYNA suite in accordance with Table 2. The measurements are from the point located in the middle of the model sample.

A table is additionally included, with the remaining parameters to be entered into the material library in LS-DYNA software, in the form of diagrams of stresses σ_{glass} to deformations ε_{glass}, stresses σ_{PVB} to deformations ε_{PVB}, the DAMAGEC variable of compressive degradation to deformations ε_{glass}, the DAMAGET variable of tensile degradation to deformations ε_{glass}, the DAMAGEC variable of compressive degradation to deformations ε_{PVB}, the DAMAGET variable of tensile degradation to deformations ε_{PVB}. Young's modulus and the Poisson ratio were determined using a Zwick/Roell Z250 universal testing machine.

3.4. Analytical model

This section presents the development of an analytical model that allows for a reliable prediction of velocities, displacements and acceleration, associated with the damage and deformation of fully clamped rectangular laminated glass subjected to a low-velocity impact. The model considers the structural strength resulting from bending, membrane and transverse shear, as well as the propagation of bending waves that change their position in the laminated glass. In addition, it was found that, due to these waves, an elastic response of the glass to low-velocity impact by rigid impactors took place. A damage criterion was used to predict crack initiation in glass panels. The individual assumptions referring to the deformation and the material reaction will be explained in detail.

3.4.1. Model approach considering the material geometry and properties

Fig. shows a piece of laminated glass schematically. It was constructed of two glass layers, glued to a composite interlayer. It was fully clamped along its four edges. The glass layers and the composite interlayer feature the same overall length: $2a$ and width $2b$, where $a \geq b$. The thickness of the outer (impacted) layer, the interlayer and the inner layer (non-impacted) is respectively h_o, h_c and h_i. The centre of the laminated glass is impacted by a spherical impactor (mass M_p, radius R_p, initial velocity v_p) perpendicularly to the outer glass layer.

The impactor is considered rigid when compared to laminated glass. When it comes to the impact of relatively large impactors: $2R_p > h_o + h_c + h_i$ on laminated glass with a medium to small thickness-to-width ratio $0.01 < (h_a + h_c + h_i)/b < 0.15$, it is worth using a thin-layer assumption that neglects local dents. The symmetry of the load reflection and the geometry is given in two longitudinal planes along $\left(x = 0, -\frac{h_c}{2} - h_o \leq z \leq \frac{h_c}{2} + h_i\right)$, as well as $\left(y = 0, -\frac{h_c}{2} - h_o \leq z \leq \frac{h_c}{2} + h_i\right)$, which makes it necessary to model only the bullet and one-fourth of the laminated glass. When it comes to a low-velocity impact: less than $9v_p$ m/s, it should be considered that the occurrence of a deformation without cracking is possible on the composite interlayer [62]. It is also assumed that the bond that occurs between the glass layer and the interlayer is sufficiently strong, so that a delamination may not occur during the entire reaction.

When the properties of the glass layer are linear and elastic, the properties of the composite interlayer (e.g. PVB) can be viscoelastic and highly deformation dependent [64.5]. However, when a low-velocity impact occurs, the stresses of the composite interlayer are not significant as opposed to its bursting stresses, and the stresses are much lower than in the glass layer, which results from much higher outer material rigidity [62,63].

We assume that the deformation of a quarter of laminated glass consists of three phases – see Fig. 5 – according to the location of the bending wave and in positive directions x and y: (1) phase one $(0 < t \leq t_1)$ – when the bending wave is initiated at the point of impact but propagates towards the boundary (velocity ξ and $\dot{\eta}$) in the positive direction x and y: (2) phase two $(t_1 < t \leq t_2)$ – bending wave in the positive direction y totals $(\eta(t) = b)$ and remains stationary at the boundary $(\dot{\eta}(t) = 0)$, then the bending wave in the positive direction x still moves in the direction of $x = a$ (i.e. $\xi < a$); (3) third phase $(t_2 < t \leq t_3)$ – when the bending wave in the positive direction, x touches the edge $(\xi(t) = a$ and $\dot{\xi}(t) = 0)$. For reasons of simplification, it is assumed that the bending wave, in the direction of y, reaches the boundary each time $y = b$, which ensues before the boundary in the direction of x, because $b < a$.

In each of the three phases, the acceptable transverse displacement area, as well as the shear deformation profiles for one-fourth of laminated glass $0 \leq x \leq \xi(t)$ and $0 \leq y \leq \eta(t)$, can be written down as follows

$$W(x,y,t) = w_0(t)\left[1 - \frac{2x^2}{\xi(t)^2} + \frac{x^3}{\xi(t)^3}\right]\left[1 - \frac{2y^2}{\eta(t)^2} + \frac{y^3}{\eta(t)^3}\right] \tag{22}$$

and

$$\gamma^0_{xz}(x,y,t) = \gamma_{xz0}(t) sin\left[\frac{\pi x}{2\xi(t)}\right] cos\left[\frac{\pi y}{2\eta(t)}\right] \tag{23}$$

$$\gamma^0_{yz}(x,y,t) = \gamma_{yz0}(t) cos\left[\frac{\pi x}{2\xi(t)}\right] sin\left[\frac{\pi y}{2\eta(t)}\right] \tag{24}$$

where five degrees of freedom are considered: shear displacements $\gamma_{xz0}(t)$ and $\gamma_{yz0}(t)$, transverse central displacement $w_0(t)$, the bending wave location in the direction $x - \xi(t)$, but also y - $\eta(t)$, which is called the Lagrange equation of the second kind. In the case of the outer area $-\xi(t) \leq x \leq \xi(t)$ and $-\eta(t) \leq y \leq \eta(t)$ (the grey area in Fig. 5), laminated glass is deemed straight: therefore $W(x,y,t) = \gamma^0_{xz}(x,y,t) = \gamma^0_{yz}(x,y,t) = 0$. It should be noted that in the case of equations (16–18) – $\xi(t)$ and $\eta(t)$, they will become a and b at the moment when the bending wave reaches the boundary, in the directions of x and y respectively.

According to Equation (16), the velocity, the transverse central displacement and the acceleration at random time t are expressed as

$$w_0(t) = W(0,0,t)v_0(t) = \dot{W}(0,0,t)a_0(t) = \ddot{W}(0,0,t) \tag{25}$$

In each of the three phases, an enforcement of the velocity, displacement and acceleration convergence conditions takes place at the point of contact $\left(x = 0, y = 0, z = -\frac{h_c}{2} - h_0\right)$ between the outer glass layer and the impactor, i.e.

$$w_p(t) = w_0(t)\dot{w}_p(t) = v_0(t)\ddot{w}_p(t) = a_0(t) \tag{26}$$

then the subscript "p" refers to the impactor.

3.4.2. Structural behaviour of individual layers

This section describes the constitutive equations for the resultant of the membrane shear force, the moment and the transverse shear force relative to the stresses of the k-th plane, i.e. $k = 1,2,3$, which refer to the outer, intermediate composite and inner glass layers, respectively. We make use of the first-order shear deformation theory of plates (the so-called Mindlin plate theory), which is based on the von Karman deformation relations, where the transverse perpendiculars will no longer be perpendicular to the central surface when it comes to a deformation. The linear constitutive relations existing between the stress and the deformation for the k-th surface of a three-layer laminate can be written as follows [64]

Table 2
New parameters for VSG glass reinforced with PVB interlayers.

RO	EG	PRG	SYG	ETG	EFG	EP	PRP	SYP	ETP	EFP
Mass density	Young's modulus for glass	Poisson's ratio for glass	Yield stress for glass	Plastic hardening for glass	Plastic strain at failure for glass	Young's modulus for polymer	Poisson's ratio for polymer	Yield stress for polymer	Plastic hardening for polymer	Plastic strain at failure for polymer
kg/m^3	*GPa*	–	*MPa*	*GPa*	–	*GPa*	–	*MPa*	*MPa*	–
2500	100	0.227	120	60	0.0004	0.253	0.435	38	3.26	2.4

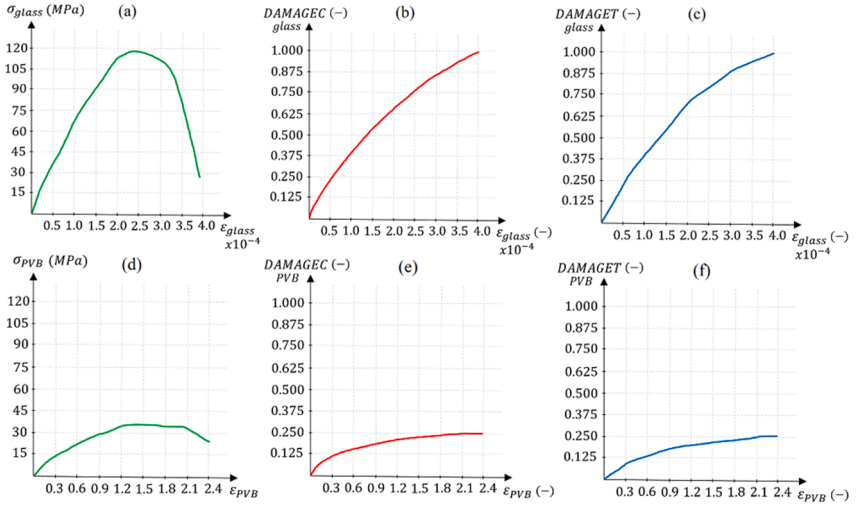

ε_{glass} [_]	σ_{glass} [MPa]	DAMAGEC [-]	DAMAGET [-]	ε_{PVB} [-]	σ_{PVB} [MPa]	DAMAGEC [-]	DAMAGET [-]
0.0	0	0	0	0.0	0	0	0
0.5×10^{-4}	32	0.21	0.23	0.3	14	0.10	0.09
0.75×10^{-4}	48	0.32	0.31	0.45	17	0.14	0.11
1.0×10^{-4}	67	0.39	0.41	0.6	21	0.15	0.14
1.25×10^{-4}	82	0.44	0.47	0.65	27	0.18	0.17
1.5×10^{-4}	90	0.53	0.53	0.9	30	0.20	0.18
1.75×10^{-4}	102	0.58	0.62	1.05	32	0.21	0.19
2.0×10^{-4}	112	0.64	0.70	1.2	35	0.22	0.20
2.25×10^{-4}	120	0.70	0.75	1.35	37	0.23	0.21
2.5×10^{-4}	116	0.76	0.79	1.5	36	0.24	0.22
2.75×10^{-4}	112	0.82	0.81	1.65	34	0.245	0.23
3.0×10^{-4}	108	0.85	0.88	1.8	33	0.247	0.24
3.25×10^{-4}	95	0.89	0.91	1.95	32	0.248	0.245
3.5×10^{-4}	76	0.93	0.95	2.1	31	0.25	0.25
3.75×10^{-4}	41	0.98	0.98	2.4	24	0.249	0.25

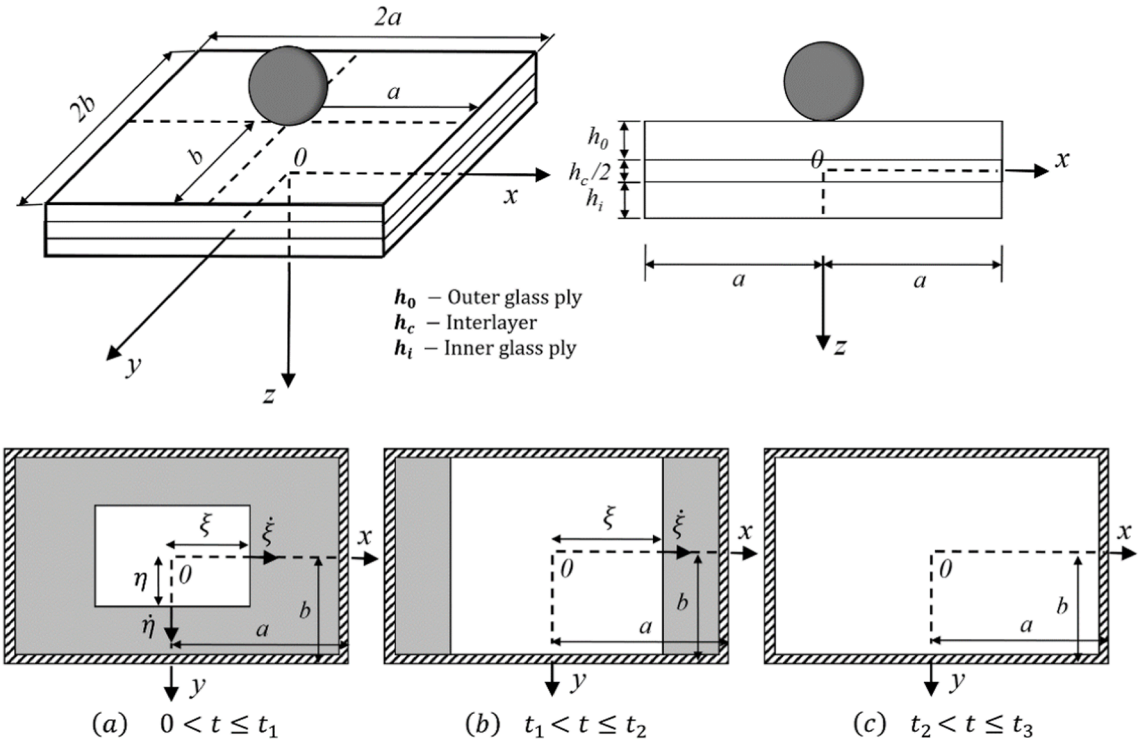

Fig. 5. Sequence of deformation phases, related to the behaviour of clamped laminated glass impacted by a rigid impactor: (a) phase one, (b) phase two, and (c) phase three. f(t) and g(t) are the position of the bending wave in the × and y directions, respectively. It is important that there was no deformation in the grey zone.

$$\begin{Bmatrix} \sigma_{xx} \\ \sigma_{yy} \\ \sigma_{yz} \\ \sigma_{xz} \\ \sigma_{xy} \end{Bmatrix}^{(k)} = \begin{Bmatrix} Q_{11} & Q_{12} & 0 & 0 & 0 \\ Q_{12} & Q_{22} & 0 & 0 & 0 \\ 0 & 0 & Q_{44} & 0 & 0 \\ 0 & 0 & 0 & Q_{44} & 0 \\ 0 & 0 & 0 & 0 & Q_{66} \end{Bmatrix}^{(k)} = \begin{Bmatrix} \epsilon_{xx} \\ \epsilon_{yy} \\ \gamma_{yz} \\ \gamma_{xz} \\ \gamma_{xy} \end{Bmatrix} \tag{27}$$

then $\sigma_{ij}^{(k)}$ are stress components; $Q_{ij}^{(k)}$ the surface rigidity reduction due to the load; $Q_{66}^{(k)} = E^{(k)}/2(1+\nu_{(k)})$, $Q_{11}^{(k)} = E^{(k)}/2(1-\nu_{(k)}^2)$, $Q_{12}^{(k)} = \nu_{(k)}Q_{11}^{(k)}$, $Q_{44}^{(k)} = Q_{11}^{(k)}$, $Q_{22}^{(k)} = Q_{11}^{(k)}$; $E^{(k)}$ expresses the Young's modulus and $\nu_{(k)}$ is the Poisson ratio.

The deformation components take the following form

$$\begin{Bmatrix} \epsilon_{xx} \\ \epsilon_{yy} \\ \gamma_{yz} \\ \gamma_{xz} \\ \gamma_{xy} \end{Bmatrix} = \begin{Bmatrix} \epsilon_{xx}^0 \\ \epsilon_{yy}^0 \\ \gamma_{yz}^0 \\ \gamma_{xz}^0 \\ \gamma_{xy}^0 \end{Bmatrix} + z \begin{Bmatrix} \epsilon_{xx}^1 \\ \epsilon_{yy}^1 \\ 0 \\ 0 \\ \gamma_{xy}^1 \end{Bmatrix} \tag{28}$$

where $\left(\epsilon_{xx}^0, \epsilon_{yy}^0, \gamma_{xy}^0\right)$ are the membrane deformations, on the basis of which the permissible displacement field function is created (see Equation (22),

$$\epsilon_{xx}^0 = \frac{1}{2}\left[\frac{\partial W(x,y,t)}{\partial x}\right]^2 \epsilon_{yy}^0 = \frac{1}{2}\left[\frac{\partial W(x,y,t)}{\partial y}\right]^2 \gamma_{xy}^0 = \frac{\partial W(x,y,t)}{\partial x}\frac{\partial W(x,y,t)}{\partial y} \tag{29}$$

and $\left(\epsilon_{xx}^1, \epsilon_{yy}^1, \gamma_{xy}^1\right)$ are the bending deformations, also called curvatures, expressed as

$$\epsilon_{xx}^1 = \frac{\partial \theta_x(x,y,t)}{\partial x} \epsilon_{yy}^1 = \frac{\partial \theta_y(x,y,t)}{\partial y} \gamma_{xy}^1 = \frac{\partial \theta_x(x,y,t)}{\partial y}\frac{\partial \theta_y(x,y,t)}{\partial x} \tag{30}$$

then the rotations of the transverse normal around the axis *y* and *x* reach accordingly

$$\theta_x(x,y,t) = \gamma_{xz}(x,y,t) - \frac{\partial W(x,y,t)}{\partial x} \theta_y(x,y,t) = \gamma_{yz}(x,y,t) - \frac{\partial W(x,y,t)}{\partial y} \tag{31}$$

Whilst in the case of the *k*-th layer the resulting forces were described as

$$\begin{Bmatrix} N_{xx} \\ N_{yy} \\ N_{xy} \end{Bmatrix}^{(k)} = \int_{z_k}^{z_{k+1}} \begin{Bmatrix} \sigma_{xx} \\ \sigma_{yy} \\ \sigma_{xy} \end{Bmatrix}^{(k)} dz \begin{Bmatrix} M_{xx} \\ M_{yy} \\ M_{xy} \end{Bmatrix}^{(k)} = \int_{z_k}^{z_{k+1}} \begin{Bmatrix} \sigma_{xx} \\ \sigma_{yy} \\ \sigma_{xy} \end{Bmatrix}^{(k)} zdz \begin{Bmatrix} Q_x \\ Q_y \end{Bmatrix}^{(k)} = \int_{z_k}^{z_{k+1}} \begin{Bmatrix} \sigma_{xz} \\ \sigma_{yz} \end{Bmatrix}^{(k)} dz. \tag{32}$$

Substituting the equations (27) as well as 28 into Equation (32) and rearranging lead to constitutive equations relating the resultant of the

membrane shear force, the transverse shear force and the moment of the stresses of the k-th plane

$$\begin{Bmatrix} N_{xx} \\ N_{yy} \\ N_{xy} \end{Bmatrix}^{(k)} = \begin{Bmatrix} A_{11} & A_{12} & 0 \\ A_{12} & A_{11} & 0 \\ 0 & 0 & A_{66} \end{Bmatrix}^{(k)} \begin{Bmatrix} \epsilon^0_{xx} \\ \epsilon^0_{yy} \\ \gamma^0_{xy} \end{Bmatrix} \begin{Bmatrix} M_{xx} \\ M_{yy} \\ M_{xy} \end{Bmatrix}^{(k)}$$
$$= \begin{Bmatrix} D_{11} & D_{12} & 0 \\ D_{12} & D_{11} & 0 \\ 0 & 0 & D_{66} \end{Bmatrix}^{(k)} \begin{Bmatrix} \epsilon^1_{xx} \\ \epsilon^1_{yy} \\ \gamma^1_{xy} \end{Bmatrix} \begin{Bmatrix} Q_x \\ Q_y \end{Bmatrix}^{(k)}$$
$$= K\frac{1-v_{(k)}}{2} \begin{Bmatrix} A_{11} & 0 \\ 0 & A_{11} \end{Bmatrix}^{(k)} \begin{Bmatrix} \gamma^0_{xz} \\ \gamma^0_{yz} \end{Bmatrix} \tag{33}$$

then K determines the shear correction factor; it is worth noting that in Mindlin plate theory $K = 5/6$ for rectangular cross-sections; $A^{(k)}_{ij}$ and $D^{(k)}_{ij}$ are the flexural and tensile rigidity specified in terms of plane rigidity $Q^{(k)}_{ij}$ as

$$\left(A_{ij}, D_{ij}\right)^{(k)} = \int_{z_k}^{z_{k+1}} Q^{(k)}_{ij}\left(1, z^2\right) dz. \tag{34}$$

3.4.3. Damage criterion

In this experiment, a crack or damage causes the glass to completely loose its load-bearing capacity. When damage occurs or all stress components drop to zero, a crack appears. Two forms of cracks exist: radial and circular cracks. Several experimental studies covered crack propagation behaviour in laminated glass [15,17,33,62,65,66]. It was then concluded that radial cracks always occurred prior to circular cracks, due to the fact that the stress from the frame is greater than radial stress [33]. Radial cracks tend to occur in a specific sequence. They occur first on the inner glass layer and then on the outer one. First, they can be observed at the point at which the laminated glass is impacted, and then it comes to crack propagation on its planes, which takes place at different speeds. As a rule, a crack spreads on the inner glass layer slower than on the outer one [17,65]. The final morphologies of radial cracks (on both sides) practically overlap each other [17].

In order to predict that a crack will occur, it is necessary to know the stress distribution in both the outer and inner glass layers. It was found that the main stress is greatest near the middle of the inner layer, i.e. $x = 0, y = 0, z = h_i + h_c/2$. Then, we assume that once this condition is met, a large-scale crack of the glass layers occurs within $0 \le x \le \xi$ and $0 \le y \le \eta$

$$D = \frac{\sigma^{(3)}_{11}(x = 0, y = 0, z = h_c + h_i/2)}{\sigma_t} = 1 \tag{35}$$

where D is the state variable that increases monotonically with the principal stress that takes place in the middle of the inner glass layer, and

$$\sigma^{(3)}_{11} \left(\triangleq \frac{\left(\sigma^{(3)}_{xx} + \sigma^{(3)}_{yy}\right)}{2} + \sqrt{\frac{\left(\sigma^{(3)}_{xx} + \sigma^{(3)}_{yy}\right)^2 + \left(\sigma^{(3)}_{xy}\right)^2}{4}} \right) \tag{36}$$

where σ_t is the maximum tensile stress. For the purpose of the study carried out, it was assumed that $\sigma_t = 200MPa$. It is also important that $D = 1$ results in a complete loss of the load bearing capacity, i.e. $Q^{(1)}_{ij} = 0$; $Q^{(3)}_{ij} = 0$.

This simplification affects the results in two ways: (1) The model assumes that glass with nonzero deformation cracks when the damage criterion is met, which leads to an excessive prediction of the loss of membrane structural, shear and flexural strength during the crack propagation on the glass planes. This ultimately leads to an overestimation of the maximum central displacement. Additionally, (2) a sudden decrease in the rigidity resulting from a reduction in the layer stress would result in a rapid regression of the compressive force or acceleration of both the laminated glass and the impactor. It was found that the crack pattern was predominantly distributed in the central sector of glass, in which the deformation occurred. Whilst the glass was not damaged where it abuts the boundary, due to slight displacements, its effect on the structural strength is small. On this basis, it is worth simplifying the damage process in the current analytical model, which was justified by the full conformity of the analytical prediction with the experimental results (this will be demonstrated in Section 3.4.5).

3.4.4. Equations of motion

The total kinetic energy of one-fourth of the laminated glass and the impactor at each possible time t can take the form

$$T = \frac{1}{2} m \int_0^b \int_0^a W^2(x, y, t) dx dy + \frac{1}{8} M_p w_p^2(t) \tag{37}$$

then, $m\left(\triangleq \rho_g h_0 + \rho_c h_c + \rho_g h_i\right)$ is the mass per unit of the laminated glass layer. The elastic deformation energy of one-fourth of the k-th laminate can be expressed as the total of the deformation energy, which is associated with the membrane, bending and shear

$$\Pi^{(k)} = \Pi^{(k)}_b + \Pi^{(k)}_m + \Pi^{(k)}_s$$
$$= \frac{1}{2}\int_0^b \int_0^a \left[M^{(k)}_{xx}\epsilon^1_{xx} + M^{(k)}_{yy}\epsilon^1_{yy} + M^{(k)}_{xy}\gamma^1_{xy} \right] dz dx dy + \frac{1}{2}\int_0^b$$
$$\times \int_0^a \left[N^{(k)}_{xx}\epsilon^0_{xx} + N^{(k)}_{yy}\epsilon^0_{yy} + N^{(k)}_{xy}\gamma^0_{xy} \right] dz dx dy + \frac{1}{2}\int_0^b$$
$$\times \int_0^a \left[Q^{(k)}_x \gamma^0_{xz} + Q^{(k)}_y \gamma^0_{yz} \right] dz dx dy. \tag{38}$$

Since the Lagrangian of the quarter of the laminated glass is

$$\mathscr{L} = T + \sum_{k=1}^{3} \Pi^{(k)} \tag{39}$$

the governing differential equations $w_0(t), \xi(t), \eta(t), \gamma_{xz0}(t), \gamma_{yz0}(t)$ are obtained by substituting the equations (37)-(39) into the general Lagrange equation of the second kind

$$\frac{d}{dt}\left(\frac{\partial \mathscr{L}}{\partial \dot{w}_0}\right) + \frac{\partial \mathscr{L}}{\partial w_0} = 0, \frac{d}{dt}\left(\frac{\partial \mathscr{L}}{\partial \dot{\xi}_0}\right) + \frac{\partial \mathscr{L}}{\partial \xi} = 0, \frac{d}{dt}\left(\frac{\partial \mathscr{L}}{\partial \dot{\eta}_0}\right) + \frac{\partial \mathscr{L}}{\partial \eta}$$
$$= 0, \frac{d}{dt}\left(\frac{\partial \mathscr{L}}{\partial \dot{\gamma}_{xz0}}\right) + \frac{\partial \mathscr{L}}{\partial \gamma_{xz0}} = 0, \frac{d}{dt}\left(\frac{\partial \mathscr{L}}{\partial \dot{\gamma}_{yz0}}\right) + \frac{\partial \mathscr{L}}{\partial \gamma_{yz0}} = 0. \tag{40}$$

These ordinary differential equations (ODEs) are solved numerically with the aid of the fourth-order Runge-Kutta method, using the following initial conditions:

$$w_0(t = 0) = 1x10^{-5} m \dot{w}_0(t = 0) = 0 \xi(t = 0) = 0.45a\dot{\xi}(t = 0) = 0 \eta(t = 0)$$
$$= 0.45b\dot{\eta}(t = 0) = 0 \tag{41}$$

It is worth noting that it is necessary to use nonzero initial values for $w_0(t = 0)$ $\xi(t = 0)$ and $\eta(t = 0)$ to avoid acceleration singularities in the case of the first numerical iteration. For reasons of simplification, it is worth assuming proportions a/b between the initial positions of the bending wave in the directions x and y, that is $\xi(t = 0)/\,/\eta(t = 0) = a/b$. Initially, a sensitivity analysis was performed to determine the impact of other values $w_0(t = 0)$, $\xi(t = 0)$ and $\eta(t = 0)$ on the structural reaction result. It became apparent that a small enough value of the central displacement was an indispensable condition for the replication $w_0 = 0$ to occur, and therefore $w_0(t = 0) = 1x10^{-5}m$ was assumed. For achieving a reasonable agreement with the experimental results in terms of the acceleration values in time (particularly the first peak at which an instantaneous cracking starts to occur), it is necessary that $\xi(t = 0)$ and

$\eta(t=0)$ are large enough. The situation in which the bending wave emanates in the vicinity of the point of impact may not occur. Then $\xi(t=0)/a = \eta(t=0)/b = 0.45$ are used throughout the entire experiment; they were obtained by means of calibration against the current experimental results.

3.4.5. Comparison of experimental results vs. Numerical model vs. Analytical model

After correct validation of the parameters of laminated glass, further tests were carried out for different amounts of individual layers of VSG and PVB interlayers. The main purpose of the research was to check the impact of the thickness and the number of individual layers of laminated glass on its strength. These tests were also used to verify the new parameters of MAT_32-LAMINATED_GLASS and MAT_112-FINITE_ELASTIC_STRAIN_PLASTICITY depending on the different configurations of the layers of glass and PVB interlayers. Additional experimental tests were carried out for a total of 40 additional samples, i.e., 20 samples for Test no. 2 and 20 samples for Test no. 3, in accordance with Table 3. They were then compared with the results of numerical simulations performed for an identical test set.

Experimental research and numerical analyses for Test no. 2 and Test no. 3 were carried out in the same way as for Test no. 1.

In Fig. 6, we present displacement, acceleration, and velocity graphs, developed on the basis of the interpolation of the values of the results obtained during the conducted 20 repetitions of the tests for each of the Test no. 1, Test no. 2, and Test no. 3.

On the basis of the comparison of experiments, numerical simulations and analytical model, it was proved that the obtained results coincide at each time point with an accuracy of up to 3.7%. Laminated glass with 5 layers of VSG glass and 4 PVB spacers demonstrated the highest strength, and its maximum displacement was 30 mm for the experimental test and 31 mm for numerical analysis. In turn, the lowest strength was recorded for laminated glass with 3 VSG glass layers and 2 PVB spacers, with 79 mm – for experi-mental test and 80 mm for numerical analysis, respectively. The obtained results are in line with our predictions and correspond to trends occurring in the scientific literature.

Therefore, we were able to confirm that the elaborated parameters for laminated glass are correct. The prediction of destruction and cracking of laminated glass obtained during experimental tests corresponds to the destruction found during numerical analyses.

3.4.6. Maximum structural response

The maximum impact response of the structure is very important for the safety of the laminated glass structure, e.g. the maximum transverse central displacement and the first peak compression force on the first glass layer. We observe that the non-dimensional maximum transverse central displacement and the non-dimensional first peak contact force indicated by

$$\overline{w}_0 = \underbrace{max}_{0\leqslant t<\infty}\left[w_0(t)/H(\triangleq h_o + h_c + h_i)\right] \tag{42}$$

and

$$\overline{F}_0 = \frac{M_p a_0(t=t_f)}{M_p g} = \frac{a_0(t=t_f)}{g} \tag{43}$$

can be expressed as a function of the following non-dimensional impact velocities, respectively

$$\lambda_1 = \left(\frac{a}{h_c}\right)^{1/4}\left(\frac{M_p V_p^2}{E_c H^3}\right)^{1/3} \tag{44}$$

and

$$\lambda_2 = \frac{H}{b}\left(\frac{E_c V_p^4}{M_p g^3}\right)^{1/3} \tag{45}$$

which were derived from the well-known Buckingham theorem. Fig. 7a and 7b prove that the parameters of the non-dimensional response $(\overline{w}_0, \overline{F}_0)$ and non-dimensional impact velocities (λ_1, λ_2) allow us to draw a single analytical curve throughout all experimental results for each PVB interlayer material over the entire configuration range of thickness and impact velocity. In addition, for each interlayer material, the predicted $\overline{w}_0$ and $\overline{F}_0$ increase in proportion to the corresponding non-dimensional impact velocities. Thus, thin laminated glass with a thin interlayer (i.e. a high value of λ_1) tends to induce a significant transverse central deformation, while the opposite (i.e. a high value of λ_2) leads to a significant first peak contact force.

Table 3
Thickness of the respective layers of laminated glass panels.

Test no.	Interlayer material	Thickness (mm)$h_{glass} + h_{PVB} + \ldots + h_{PVB} + h_{glass}$	Impact velocity (m/s)
1	PVB	20 + 2.28 + 20 + 2.28 + 20	10.00
2	PVB	15 + 2.28 + 15 + 2.28 + 15 + 2.28 + 15	10.00
3	PVB	12 + 2.28 + 12 + 2.28 + 12 + 2.28 + 12 + 2.28 + 12	10.00

4. Crash tests of a standard vehicle impact into a wall of laminated glass

4.1. Experimental setup

In the subsequent stage of our research we verified the parameters of VSG glass with vinyl PVB interlayers obtained during validation. The main purpose of the tests was to check the reliability of the obtained strength parameters of the laminated glass loaded with an impacting vehicle.

The essence of verification is to transform the mathematical model into a physical model that maps the behaviour of the actual material precisely, effectively, and realistically. During the next approximation verification (using model parameters), the output data is matched to the input data. In other words, the first unregulated numerical model is used to solve a relatively simple problem with a known result obtained during experiments. Knowing the result "in advance", it is possible to assess and compare whether the result of the analysis using the model is consistent with it, i.e., whether the verification was successful (and we can initiate the application of the model) or there are discrepancies – when another approach is required using a different configuration of model parameters.

The verification procedure consisted of successive iterative simulations, the purpose of which is to determine the size of the parameters to be verified, so that the output data obtained during the simulation in the LS-DYNA suite are as consistent, as possible with the input data obtained based on laboratory tests. Verification of parameters determining the properties of laminated glass MAT_32-LAMINATED_GLASS and MAT_112-FINITE_ELASTIC_STRAIN_PLA- STICITY included the calibration of parameters obtained in Table 2, which were obtained during the validation of VSG glass and PVB interlayers parameters.

In order to carry out the crash tests used to verify the parameters, an original test bench was constructed in the laboratory of the Gdansk University of Technology. The diagram of the test bench for crash tests is presented in Fig. 8.

The test bench was constructed in four stages. The first stage involved the construction of a vehicle parking platform. The platform was set at a height of 5 m and was made as a pole steel structure on which steel beams were supported. The individual elements of the structure had an H-shaped cross-section. A steel plate was attached to

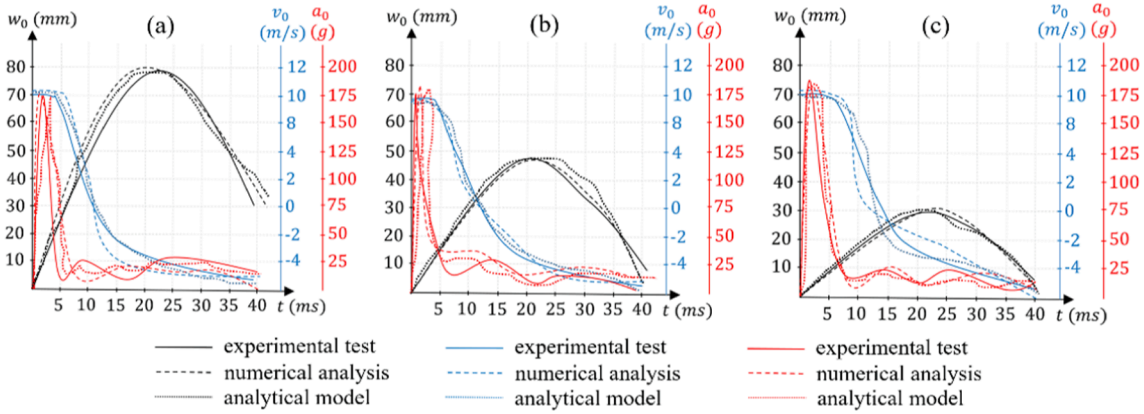

Fig. 6. Comparison of the results of experimental tests and numerical analyses based on the interpolation of the values of the results for: 20 samples from (a) Test no.1, 20 samples from (b) Test no. 2, and 20 samples from (c) Test no. 3.

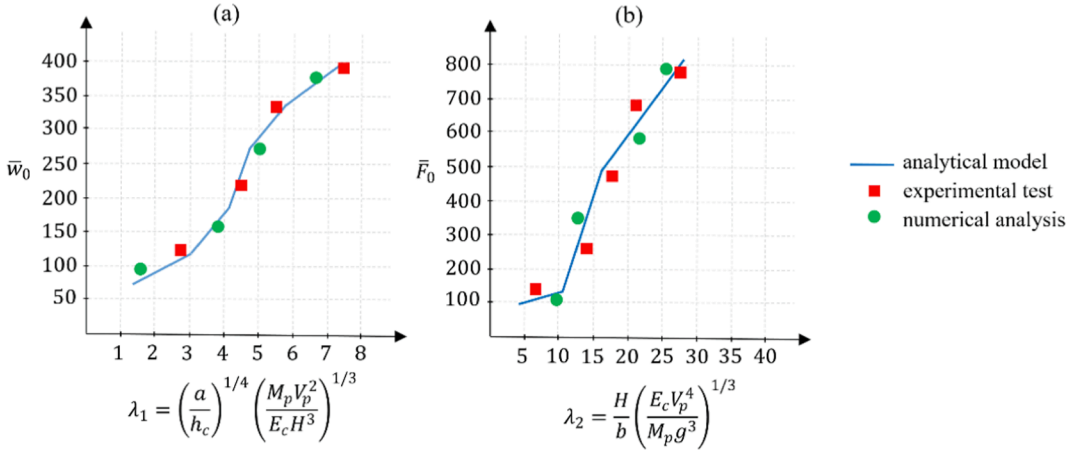

Fig. 7. Analytical predictions, numerical analysis and experimental results of non-dimensional (a) maximum transverse central displacement and (b) maximum contact force.

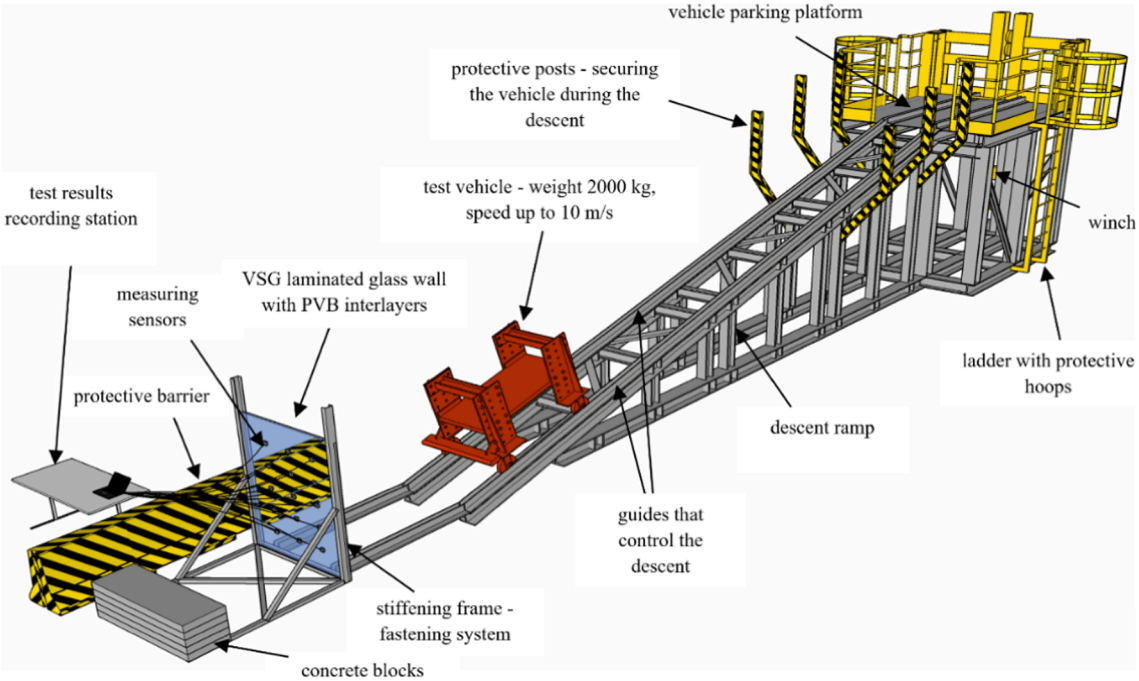

Fig. 8. Diagram of the test bench for conducting crash tests.

the support beams. The entire structure was strengthened with secondary elements. Around the plat-form, safety barriers were erected at a height of min. 1 m. On one side, a ladder with protective shielding was constructed in order to allow access to the platform. The platform also included guides on where the vehicle was placed. An electric winch was installed at the rear wall of the vehicle parking platform, whose task was to pull the vehicle back onto the platform after the crash test.

In the second stage, we constructed a ramp, which enables the vehicle to gather speed. The structure of the ramp was also supported with steel columns with an H-shaped cross-section. The highest pole will be at the parking platform of the vehicle, while the subsequent poles had a decreasing height towards the other end of the ramp. The main support beams with an H-shaped cross-section, on which guides enabling a controlled passage of the vehicle were mounted, were supported on the poles. The supporting beams of the ramp were concentrated with secondary elements in order to maintain the overall stability of the structure. The total length of the ramp was 20 m, while the longitudinal slope was over 30%. In addition, in order to secure the passage on the highest poles, there were protections installed to prevent the vehicle from falling from a high height (Figs. 9a and 10.

The third stage of construction was the execution of a collision and measurement stand located at the end of the ramp. In order to fix the wall sample of laminated glass, a rigid steel frame with a width of 1500 mm and a height of 1800 mm was made. The steel frame consisted of U-shaped profiles. The samples were inserted in the profiles and then reinforced with the use of special screw-in clamps covered with rubber caps. The steel frame was secured at the rear against displacement using heavy concrete blocks. At the crash-test and measurement station, a location was prepared to enable the safe placement of the device used to perform and record measurements, sensors, and a dedicated computer. Additionally, a high-speed video camera was installed to record the entire course of the crash test.

The final, fourth stage involved the construction of a test vehicle. The vehicle, with an average mass of a loaded car of approx. 2000 kg, and the average width of an actual car, which was some 1.8 m. The bumper of the test vehicle was a replaceable element, which allowed for the installation of bumpers of different widths. This allowed us to achieve an appropriate impact area, dedicated to different sample widths. The vehicle was made entirely of steel as a two-axle, four-wheel vehicle. The mass of the vehicle could be increased by adding an additional load on the plate mounted in the middle (Fig. 9b).

Experiments were carried out for a total of 20 samples in accordance with Table 4. The test vehicle reached a speed of 10 m/s at the moment of impact against the sample. During the experiments, measurements of stresses, deformations, displacements, degradation at compression, and tensile and impact force were performed. These data were collected by sensors placed on the tested wall. In addition, the speed and vehicle delay were also recorded, as well as a high-speed video camera crash test recording was performed.

Table 4
Thickness of the respective layers of laminated glass and speed of the test vehicle.

Test no.	Interlayer material	Thickness (mm)$h_{glass} + h_{PVB} + \ldots + h_{PVB} + h_{glass}$	Impact velocity (m/s)
1	PVB	20 + 2.28 + 20 + 2.28 + 20	10.00

Fig. 9. View of (a) the crash test bench and (b) the test vehicle.

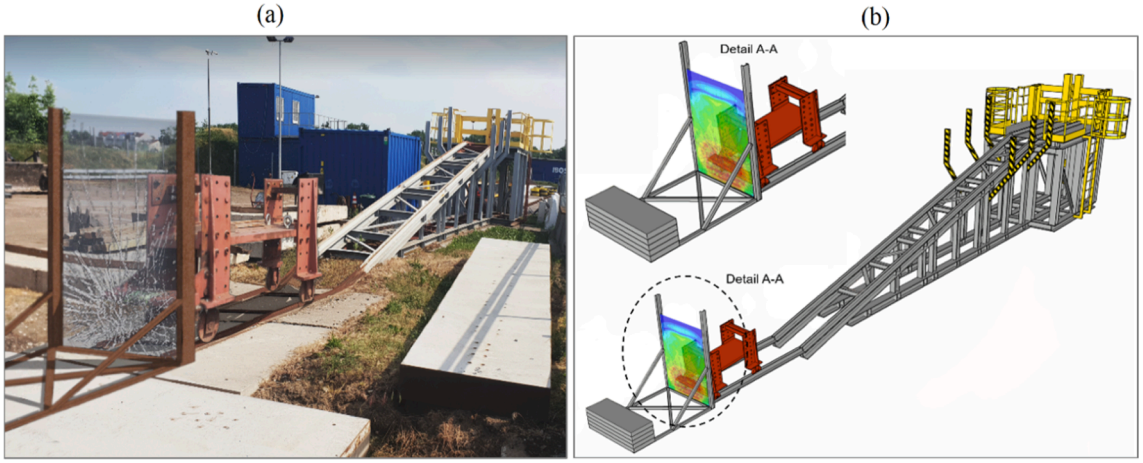

Fig. 10. Comparison of the results of (a) experimental tests and (b) numerical tests for the sample with Test no. 1.

The conducted experimental research formed the basis for the preparation of the numerical model.

4.2. Numerical simulation

Numerical modelling of the impact of the test vehicle against the wall of laminated glass, taking into account the strength criterion of cracking, was performed in a software suite for the study of fast-changing phenomena called the LS-DYNA. We constructed an identical test bench including the same vehicle, with an accuracy close to 1:1 in relation to the experimental test, in the said suite. The update of the FEM model was performed on the basis of the results of laboratory tests for an identically executed model of walls made of VSG laminated glass reinforced with vinyl interlayers. The measurement points were a reflection of the places where the results from the experiment were read.

The material MAT_32-LAMINATED_GLASS and MAT_112-FINITE_ELASTIC_STRAIN_PLASTICITY was assigned to the FE model of the laminated GLASS sample. The energy release rates of glass are 10 N/m for mode I and 50 N/m for modes II and III [33]. The PVB was modelled using the Mooney-Rivlin constitutive model with the corresponding constants A = 1.6 MPa and B = 0.06 MPa [21]. The parameters of the intrinsic cohesive model for the modelling of the adhesion are $\psi_n = \psi_t = 100N/m$ and $\delta_n = \delta_t = 0.001mm$ [43].

Strain-rate sensitivity (SRS) of flow stress is an important parameter for the deformation mechanism of materials. Strain rate sensitivity was taken into account in the Mooney-Rivlin model. The Mooney-Rivlin model is able to correctly describe the behaviour of the PVB material in case of significant deformations and deformation speeds of from 100 to 5000 s^{-1}. The strain rates range from 100 to 5000 s^{-1} are able to cover the range of strain rates of PVB material in the impact damage process of laminated glass walls at the speeds of 120 km/h and below.

Numerical calculations were performed using the Explicite procedure. Due to the small step of integrating the equations of motion over time, as well as the ES mesh wall adopted for modelling, with a small size consisting of 8 nodal cubic brick elements of reduced integration with a linear function of the C3D8R shape, performing the calculations necessitated high computing power. We select brick elements instead of shell elements for glass in order to model the crack propagations through the glass thickness. PVB film is discretized into brick finite elements because it is prone to large deformation. The advantages of brick elements over tetrahedral elements are primarily higher accuracy. The size of the FEM mesh was 1 mm in the ×, y, and z directions, respectively. The convergence criterion assumed for defining the best mesh discretization was adopted based on displacement at point. The grid size was considered correct when the difference in the displacement results, at the point between the two grid pitch sizes, was approx. 2%. The numerical model contained 2 954 679 brick elements. We used the Triton supercomputer available in CI TASK at the Gdansk University of Technology to perform the numerical calculations.

The results obtained during experimental and numerical research were compared and presented in Fig. 8.

4.3. Results

Based on the obtained results, we found that the damage to the laminated glass panel caused during experiments was identical to the damage that was obtained during numerical simulations. After comparing the resulting scratches and cracks of the glass, we proved that they overlap with an accuracy of 1.2 mm.

In Fig. 11, we presented the results in the form of graphs elaborated on the basis of interpolation of the values of the results obtained during the 20 repetitions of the sample from Table 4.

We proved that it is possible to effectively and efficiently verify the parameters of the model of PVB interlayers reinforced VSG glass. The results acquired during experimental research and numerical calculations coincide at virtually every point in time, and the maximum difference between the resulting values is less than 2.9%. The maximum glass tension σ_{glass} amounted to approx. 116 MPa with a deformation ε_{glass} of approx. 0.00039, for which the compression degradation variable *DAMAGEC* and the tensile degradation variable was 1.000. However, the

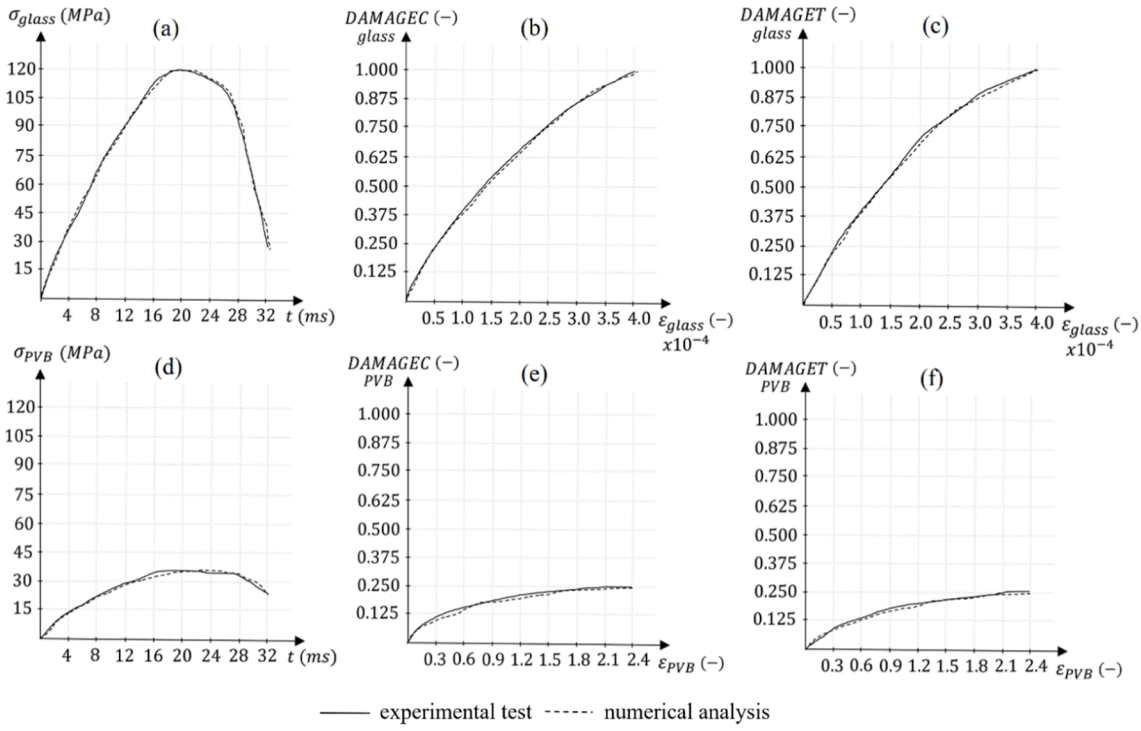

Fig. 11. Comparison of the results of experimental tests and numerical simulations based on the interpolation of the values of the results for 20 repetitions of sample destruction for Test no.1 – Table 4.

maximum PVB stresses σ_{PVB} amounted to approx. 36 MPa with a deformation ε_{PVB} of approx. 2.30, for which the compression degradation variable *DAMAGEC* and the tensile degradation variable were 0.270.

Therefore, we were able to confirm that the elaborated parameters for laminated glass are correct. The prediction of destruction and cracking of laminated glass obtained during experimental tests corresponds to the destruction found during numerical analyses.

Based on the obtained results, the parameters of laminated glass were calibrated to constitute an input file for MAT_32-LAMINATED_GLASS and MAT_112-FINITE_ELASTIC_STRAIN_PLASTICITY implemented in the material database in the LS-DYNA suite in accordance with Table 2.

4.4. Influence of temperature on a laminated glass wall

After correct verification of the parameters of laminated glass, further tests were carried out for different amounts of individual layers of VSG and PVB interlayers. The wall adopted for the experiment had the shape of a rectangle with a width of 1500 mm and a height of 1800 mm, and its was also assigned parameters in accordance with Table 5. The total thickness was 60 mm. In order to assess the impact of the thickness of individual layers of glass and the film interlayers separating them, on the strength of the wall, we performed crash tests for 3 types of walls (Fig. 12).

The first (#1) of them was made as a wall consisting of 3 layers of laminated glass with a thickness of one layer equal to 20 mm + 2 film interlayers with a thickness of 2.28 mm each.

The second (#2) wall had 4 layers of glass with a thickness of one layer of 15 mm + 3 film interlayers with a thickness of 2.28 mm each.

The third (#3) wall was made of 5 layers of glass with a thickness of 12 mm each + 4 film interlayers with a thickness of 2.28 mm each. The thickness of the film interlayers was not counted towards the total wall thickness.

Experimental research and numerical analyses for Test no. 2 and Test no. 3 were carried out in the same way as Test no. 1 from Table 4.

The tests were carried out in various atmospheric conditions. Thermal effects were included using the sequential coupling implemented in the code using COUPLED THERMAL-ELECTRICAL and THERMAL_EXPANSION. In Fig. 13 we present graphs of displacement as a function of time developed on the basis of the interpolation of the values of the results obtained during the 20 repeated tests carried out at 25 °C (summer), 20 tests at 0 °C (neutral), and 20 tests at −25 °C (winter) for each corresponding test, Test no. 1, Test no. 2, and Test no. 3, respectively.

On the basis of the comparison of experiments and numerical simulations, it was found that the obtained results coincide at each time point with an accuracy of up to 2.8%.

The laminated glass with 5 layers of VSG glass and 4 PVB interlayers demonstrated the highest strength, and its maximum displacement was 210 mm (25 °C), 145 mm (0 °C), and 78 mm (-25 °C) – for the experimental test and 208 mm (25 °C), 144 mm (0 °C), and 79 mm (-25 °C) – for the numerical analysis. The lowest strength was demonstrated by the laminated glass with 3 layers of VSG glass and 2 PVB interlayers, with respectively 123 mm (25 °C), 82 mm (0 °C), and 39 mm (-25 °C) – for the experimental test and 125 mm (25 °C), 80 mm (0 °C), and 38 mm (-25 °C) – for the numerical analysis.

PVB is a viscoelastic material. A viscoelastic material is one whose physical properties depend on the temperature and duration of the load. At room temperature, PVB is a soft material and only an elongation greater than the limit value causes its destruction. At low temperatures (below 0 °C) and under short-term loads, PVB interlayers are able to transfer full shear stresses between the layers of glass. However, at high temperatures and long-term loads, these properties are reduced.

5. Crash tests of a real car impact into a wall of laminated glass

5.1. Experimental and numerical simulation setup

During the last stage of the research, after correct validation and verification of the parameters of VSG glass reinforced with PVB interlayers, experimental and numerical tests of the impact of a typical passenger car against a wall constituting the passive protection system of the building were carried out (Fig. 14).

The tests were carried out on the basis of the newly obtained parameters for laminated glass. We used a Toyota passenger car for crash tests for the experiment and numerical simulations. The car was complete, i.e., it had all the elements of the chassis and body, as well as complete equipment including the engine. The vehicle was operational. The numerical model of the car was entirely made in the LS-DYNA suite and corresponded to the construction of the car, which was used during the experiment with the accuracy of modelling the details equal to 1:1.

Experimental tests and numerical simulations of the impact of a motor vehicle were carried out for different thicknesses of glass layers and different numbers of PVB interlayers in accordance with Table 5.

The task was divided into 3 stages:

- **#A:** performing tests for a wall with a thickness of 60 mm: 3 layers of laminated glass with a thickness of 20 mm each + 2 PVB interlayers with a thickness of 2.28 mm each – repeated for: 10 samples at an impact speed v_{max} = 50 km/h, 10 samples at impact speed v_{max} = 75 km/h, and 10 samples at impact speed v_{max} = 100 km/h
- **#B:** performing tests for a wall with a thickness of 60 mm: 4 layers of laminated glass with a thickness of 15 mm each + 3 PVB interlayers with a thickness of 2.28 mm each – repeated for: 10 samples at an impact speed v_{max} = 50 km/h, 10 samples at impact speed v_{max} = 75 km/h, and 10 samples at impact speed v_{max} = 100 km/h
- **#C:** performing tests for a wall with a thickness of 60 mm: 5 layers of laminated glass with a thickness of 12 mm each + 4 PVB interlayers

Table 5
Parameters of samples used in crash tests.

No	Study type	Wall model	Wall dimensions (width × height	Wall thickness	Glass layers thickness	Foil spacers layers thickness	V vehicle	Vehicle impact angle
No.	*[-]*	*Sketch*	*[mm]*	*[mm]*	*[mm]*	*[mm]*	*[km/h]*	*[°]*
#A	CRASH TEST- expirmental-numerical		2200X3000	60	3 × 20	2 × 2,28	50	0
							75	0
	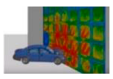						100	0
#B			2200X3000	60	4 x15	3 × 2,28	50	0
							75	0
							100	0
#C			2200X3000	60	5 × 12	4 × 2,28	50	0
							75	0
							100	0

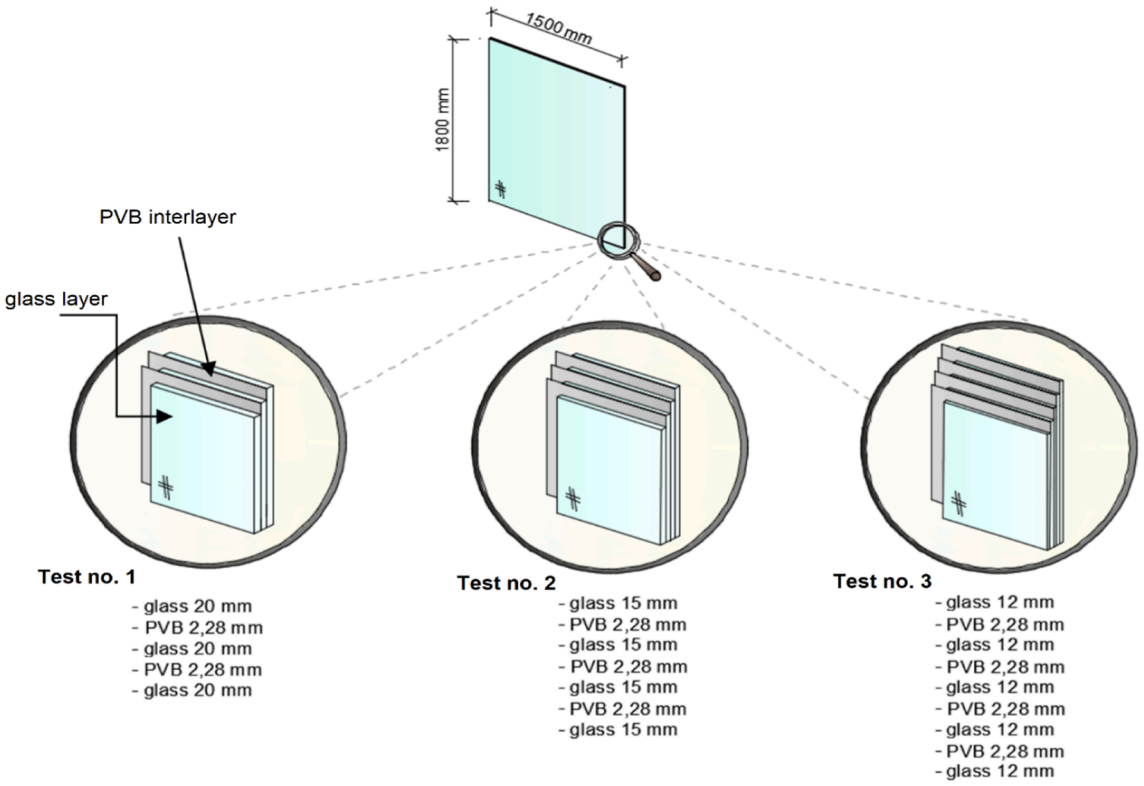

Fig. 12. Thickness of individual layers of laminated glass panels.

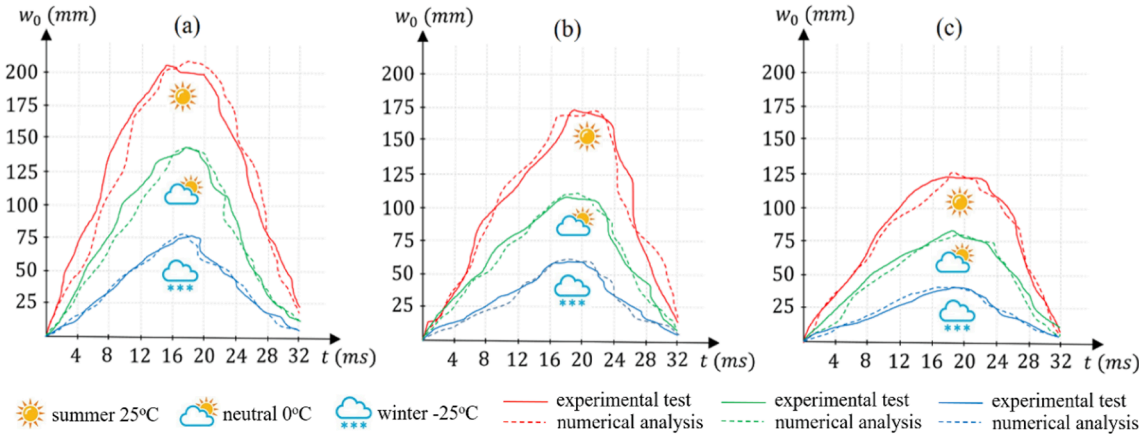

Fig. 13. Comparison of the results of experimental tests and numerical analyses based on the interpolation of the values of the results for: 20 samples from (a) Test no.1, 20 samples from (b) Test no. 2, and 20 samples from (c) Test no. 3.

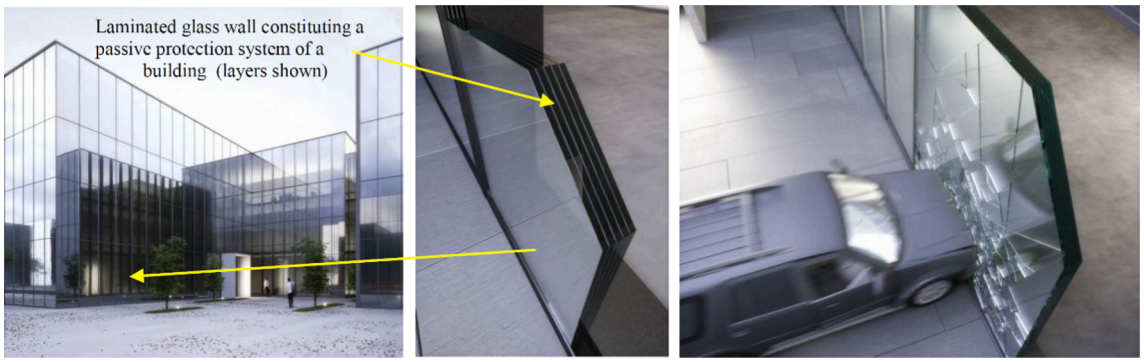

Fig. 14. An example of using a laminated glass wall that is a passive building protection system – visualization. (author's own project).

with a thickness of 2.28 mm each – repeated for: 10 samples at an impact speed $v_{max} = 50$ km/h, 10 samples at impact speed $v_{max} = 75$ km/h, and 10 samples at impact speed $v_{max} = 100$ km/h

The vehicle impact angle was set to 0°, i.e., the car impacted in a direction perpendicular to the laminated glass wall.

During the tests, it was very important to take into account the impact of the fastening frame and the assembly substructure on the amount of dissipated energy generated during the impact. In the experimental tests the laminated glass wall has been fixed on four edges using a U-shaped welded steel structure. The sample was clamped on the left and right edges using 18 bolts (9 bolts on left side, 9 bolts on right side). The top and bottom edges was clamped using 22 (11 bolts on each side). Whereas during the numerical simulation the laminated glass wall has been fixed on four edges using fixed boundary conditions (Fig. 15). The laminated glass wall had to be restrained on all sides, to prevent the car from driving inside with it.

The material MAT_32-LAMINATED_GLASS and MAT_112-FINITE_ELASTIC_STRAIN_PLASTICITY was used for the FE model of the laminated glass wall, to which the parameters from Table 2 were assigned. The energy release rates of glass are 10 N/m for mode I and 50 N/m for modes II and III [33]. The PVB was modelled using the Mooney-Rivlin constitutive model with the corresponding constants A = 1.6 MPa and B = 0.06 MPa [21]. The parameters of the intrinsic cohesive model for the modelling of the adhesion are $\psi_n = \psi_t = 100N/m$ and $\delta_n = \delta_t = 0.001mm$ [43]. Strain-rate sensitivity (SRS) of flow stress is an important parameter for the deformation mechanism of materials. Strain rate sensitivity was taken into account in the Mooney-Rivlin model. The Mooney-Rivlin model is able to correctly describe the behaviour of the PVB material in case of significant deformations and deformation speeds of from 100 to 5000 s^{-1}. The strain rates range from 100 to 5000 s^{-1} are able to cover the range of strain rates of PVB material in the impact damage process of laminated glass walls at the speeds of 120 km/h and below.The FE model was formed of 8 nodal cubic elements of reduced integration with a linear function of the C3D8R shape. We select brick elements instead of shell elements for glass in order to model the crack propagations through the glass thickness. PVB film is discretized into brick finite elements because it is prone to large deformation. The advantages of brick elements over tetrahedral elements are primarily higher accuracy. The size of the FEM mesh was 1 mm in the ×, y, and z directions, respectively. The convergence criterion assumed for defining the best mesh discretization was adopted based on displacement at point. The grid size was considered correct when the difference in the displacement results at the point between the two grid pitch sizes was approx. 2%. The numerical model contained 3 467 900 brick elements.

Numerical calculations necessitated high computing power due to the very accurate FEM numerical model of the car, the small size of the ES mesh for the wall made of laminated glass with PVB interlayers, as well as the need to adopt a very small step of integration over time. Therefore, the final numerical simulations of the crash tests were carried out on the Tryton high-power supercomputer (HPSC) available at the Gdansk University of Technology laboratory.

5.2. Results

In Fig. 16 we present the results obtained during the experimental research recorded by the installed high-speed video camera, which recorded the entire course of the crash test.

In Fig. 17 we present the results obtained during numerical simulations of the crash test. The key of stress maps was unified for all views of the moment of impact at a given point in time. The reason for this was to enable an illustrative analysis of the progressive prediction of cracking and destruction of the laminated glass wall.

The prediction of damage to the laminated glass wall for samples #A, #B and #C obtained during the crash test is analogous to both experiments and numerical simulations. The scratches and cracks of the glass that resulted from the impact with the car coincide, with an accuracy of 4 mm, between the experiment and the FEM model.

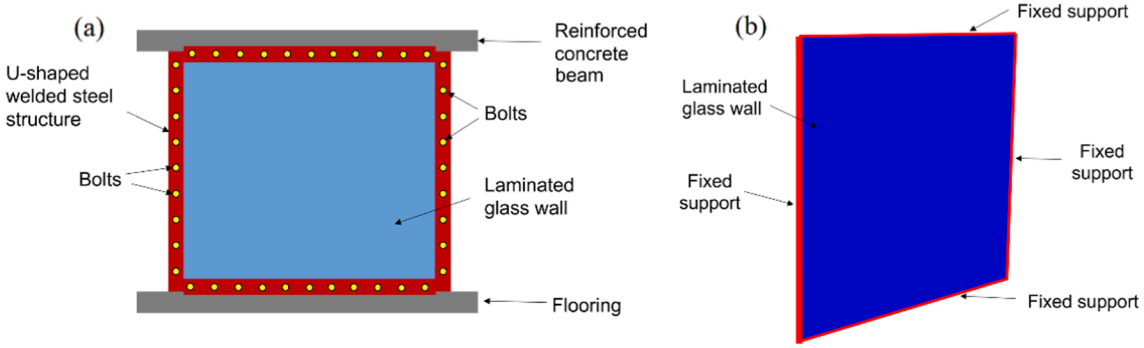

Fig. 15. Boundary conditions: (a) experimental tests, (b) numerical analysis.

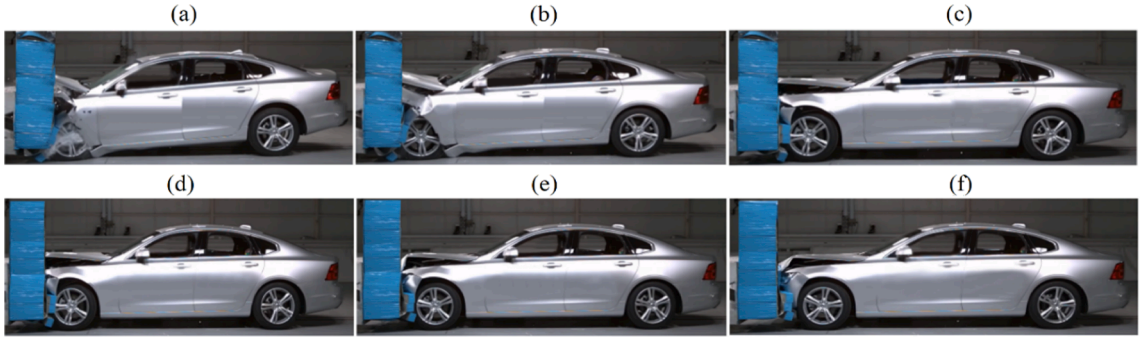

Fig. 16. Experimental studies of damage to laminated glass walls (sample #C) under the influence of car impact at a speed of 100 km/h: (a) view at 12 ms, (b) view at 10 ms, (c) view at 8 ms, (d) view at 6 ms, (e) view at 4 ms, (f) view at 2 ms.

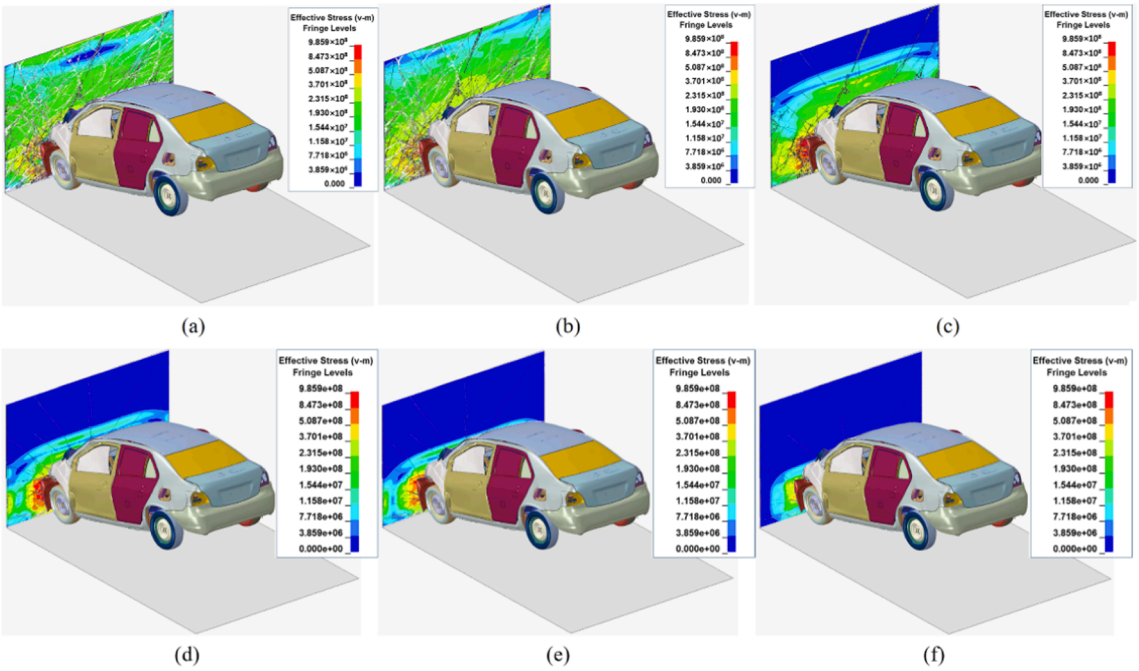

Fig. 17. Numerical simulations of damage to laminated glass walls (sample #C) under the influence of car impact at a speed of 100 km/h: (a) view at 11 ms, (b) view at 9 ms, (c) view at 7 ms, (d) view at 6 ms, (e) view at 4 ms, (f) view at 2 ms.

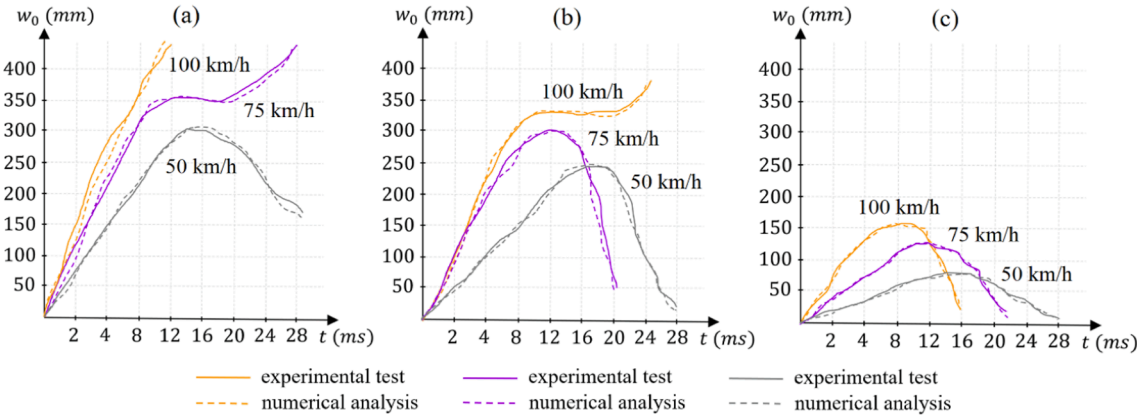

Fig. 18. Comparison of the results of experiments and numerical tests of the destruction of the VSG wall with PVB interlayers: (a) sample #A, (b) sample #B, (c) sample #C.

In Fig. 18, time displacement graphs developed on the basis of interpolation of the values of the results obtained during 30 repetitions of tests for sample #A at impact speeds of v_{max} = 50 km/h (10 repetitions), 75 km/h (10 repetitions), and 100 km/h (10 repetitions), 30 repetitions of tests for sample #B at impact speeds v_{max} = 50 km/h (10 repetitions), 75 km/h (10 repetitions), and 100 km/h (10 repetitions), and 30 repetitions of tests for sample #C at impact speeds v_{max} = 50 km/h (10 repetitions), 75 km/h (10 repetitions), and 100 km/h (3 repetitions) were provided.

On the basis of the comparison of experiments and numerical simulations, it was found that the obtained results coincide at each time point with an accuracy of up to 2.5%.

The strength of the VSG laminated glass wall with PVB interlayers was estimated de-pending on the thickness of the glass layers and the number of PVB interlayers. It was proven that the laminated glass wall with 3 layers of glass with a thickness of one layer equal to 20 mm + 2 PVB interlayers with a thickness of 2.28 mm had the lowest load-bearing capacity, as expected. At 100 km/h and 75 km/h, the wall was completely destroyed and the car penetrated it. The maximum displacement exceeded 400 mm. It was only at a speed of 50 km/h that the car was stopped by the wall of constructed laminated glass, and the maximum displacement reached the value of 300 mm. The wall of laminated glass with 4 layers of glass with a thickness of one layer equal to 15 mm + 3 PVB interlayers with a thickness of 2.28 mm was destroyed at a speed of 100 km/h, for which the maximum displacement exceeded 350 mm, while at speeds of 75 km/h and 50 km/h, the car was stopped by the wall structure reaching the maximum displacement value of 300 mm and 245 mm, respectively. The highest strength was observed for the laminated glass wall with 5 layers of glass with a thickness of one layer equal to 12 mm + 4 PVB interlayers with a thickness of 2.28 mm, which met the conditions of load-bearing capacity for the car impacting at speeds of 50 km/h – with maximum displacement value of 75 mm, 75 km/h – maximum displacement value of 125 mm, and 100 km/h – maximum displacement value of 160 mm.

Considering the above results, it was discovered that the addition of another PVB interlayer increased the load-bearing capacity of the laminated glass wall. It was also noted that the use of a minimum of 4 PVB interlayers with a thickness of 2.28 mm of PVB spacers results in a

disproportionately greater increase in load-bearing capacity than in the case of the use of 3 interlayers or less. However, one should be aware that adding interlayers is also associated with the addition of an additional layer of glass, which in turn causes a rapid increase in the weight of the entire wall. Economic and technical considerations should also be taken into account when designing laminated glass walls. The higher the weight of the wall, the more expensive the transport and installation, and also the larger steel fastenings to which the glass panes of the wall are mounted.

6. Conclusions

We developed an analytical model intended for the prediction of damage and deformation of fully clamped rectangular-shaped laminated glass when subjected to high-velocity impact. Additionally, this was verified by us. The model considers the bending wave propagation and significant deformations as well as the effects of the transversal and membrane shear and bending. Large-scale cracks on the glass planes were formed, based on the stress damage assumption. The analytical model was validated by confronting its estimates with the experimental data. It was found that there was a good correlation between the wide impact velocity amplitude and the PVB laminated glass thickness configuration. The use of a more rigid interlayer material was proven to result in an increased contact force as well as a lower transversal displacement in the laminated glass interlayer. For regulating the first peak contact force as well as the non-dimensional maximum transverse central displacement during the impact response, two groups of non-dimensional impact velocities were used. It was found that thin laminated glass with a thin interlayer featured a small first peak contact force and a significant maximum *trans*-verse central displacement.

Based on the acquired results, we proved that it was possible to effectively and efficiently develop the material parameters of laminated glass. The conducted procedure of validation and verification of parameters can be considered correct, as the results of experimental and numerical tests coincided with an absolute error that was not larger than 3.7%. Therefore, new strength parameters of laminated glass with PVB vinyl interlayers were clearly indicated and identified, and the method of obtaining them was determined. These parameters were proved to very accurately reflect the mechanics of glass cracking in the non-elastic range under the impact of a motor vehicle depending on the prevailing weather conditions and air temperature. The new parameters of laminated glass can be implemented as a ready-made input.mat file of the material available in the material library under the name MAT_32-LAMINATED_GLASS and MAT_112-FINITE_ELASTIC_STRAIN_PLASTICITY in the LS-DYNA suite.

A thorough analysis of the prediction of damage to walls made of laminated VSG glass with PVB interlayers under conditions of impact of a motor vehicle is complicated. Numerical methods based on fast-changing dynamic phenomena, including the finite element method, seem to be powerful tools for such analysis. Finite element models may describe the geometry and properties of laminated glass walls with sufficient accuracy. The analysis presented in this article and the acquired results allow us to estimate the strength of VSG glass walls reinforced with PVB interlayers, depending on the number of layers of glass and interlayers.

On the basis of the obtained results, we found that its strength depends on the number of PVB interlayers. The use of a passive protection system in form of a laminated glass wall with an appropriate number of interlayers, i.e., at least 4 pieces of PVB interlayers, can ensure safety against the impact of a motor vehicle at a speed of 100 km/h. The multi-layered structure of laminated glass, consisting of many panes, results in a more favourable behaviour after breaking and absorbs more energy during destruction. Additionally, the use of only one interlayer increases the strength of the wall from 200% to 300%, be-cause the interlayer, as a viscoelastic material, is able to transfer shear stresses between individual layers of glass.

Based on the extensive review of the subject literature, we can conclude that the com-prehensive calibration of the strength parameters of laminated glass under the influence of a car impact was not carried out thus far, at least not as a complete analysis. On this basis, we concluded that the newly elaborated parameters of laminated glass broaden and significantly enrich the issue of the analysis of construction structures.

Considering the above aspects, it should be stated that the objective of the present work has been achieved, which is confirmed by numerous experimental studies and numerical analyses. The proposed analytical approach is an effective and reliable design tool for damage assessment engineers who would prefer analytical models rather than a full-scale FE analysis, which usually involves a significant cost to calculate. Research aimed at creating rules for the design of safety systems based on the possibility of using laminated glass walls as a building passive protection system with a glass-clad ground floor should be treated as a priority, and the results obtained should be disseminated in the environment of architects and constructors.

Funding

The research was financed on the basis of the obtained research and development grant of INVEST-STEEL Sp. z o.o. company with the number IS/0001/2021.

CRediT authorship contribution statement

Karol Grębowski: Data curation, Writing – original draft, Conceptualization, Methodology, Software, Investigation, Supervision, Validation, Writing – review & editing. **Monika Zielińska:** Data curation, Writing – original draft, Conceptualization, Methodology, Software, Investigation, Supervision, Validation, Writing – review & editing.

Declaration of Competing Interest

The authors declare that they have no known competing financial interests or personal relationships that could have appeared to influence the work reported in this paper.

Data availability

The authors do not have permission to share data.

References

[1] Qipeng M, Liwei W, Huang D. An extended peridynamic model for dynamic fracture of laminated glass considering interfacial debonding. Compos Struct 2022; 150:115552.
[2] Chen S, Zang M, Wang D, Zheng Z, Zhao C. Finite element modelling of impact damage in polyvinyl butyral laminated glass. Compos Struct 2016;138:1–11.
[3] Eisenträger J, Naumenko K, Altenbach H, Meenen J. A user-defined finite element for laminated glass panels and photovoltaic modules based on a layerwise theory. Compos Struct 2015;133:265–77.
[4] Wenju L, Yanchao S, Hong H, Xihong Z. Numerical analysis of dynamic responses of laminated glass window subjected to gas explosions. Eng Struct 2021;238: 112243.
[5] Foraboschi P. Analytical model for laminated-glass plate. Compos B Eng 2012;43: 2094–106.
[6] Foraboschi P. Hybrid laminated-glass plate: design and assessment. Compos Struct 2013;106:250–63.
[7] Castori G, Speranzini E. Structural analysis of failure behavior of laminated glass. Compos B Eng 2017;125:89–99.
[8] Overend M, Butchart C, Lambert H, Prassas M. The mechanical performance of laminated hybrid-glass units. Compos Struct 2014;110:163–73.
[9] Bennison SJ, Jagota A, Smith CA. Fracture of glass/poly (vinyl butyral) (Butacite) laminates in biaxial flexure. J Am Ceram Soc 1999;82:1761–70.
[10] Larcher M, Solomos G, Casadei F, Gebbeken N. Experimental and numerical investigations of laminated glass subjected to blast loading. Int J Impact Eng 2012; 39:42–50.
[11] Xu J, Li Y, Liu B, Zhu M, Ge D. Experimental study on mechanical behavior of PVB laminated glass under quasi-static and dynamic loadings. Compos Part B: Eng 2011;42:302–8.
[12] Osnes K, Hopperstad S, Børvik T. Rate dependent fracture of monolithic and laminated glass: Experiments and simulations. Eng Struct 2022;212:110516.

[13] Amadio C, Bedon C. Buckling of laminated glass elements in out-of-plane bending. Eng Struct 2010;32:3780–8.
[14] Xu J, Sun Y, Liu B, Zhu M, Yao X, Yan Y, et al. Experimental and macroscopic investigation of dynamic crack patterns in PVB laminated glass sheets subject to light-weight impact. Eng Fail Anal 2011;18:1605–12.
[15] Chen J, Xu J, Liu B, Yao X, Li Y. Quantity effect of radial cracks on the cracking propagation behavior and the crack morphology. PLoS One 2014;9:e98196.
[16] Aenlle M, Pelayo F, Ismael G. An effective thickness to estimate stresses in laminated glass beams under dynamic loadings. Compos B Eng 2015;82:1–12.
[17] Chen J, Xu J, Yao X, Xu X, Liu B, Li Y. Different driving mechanisms of in-plane cracking on two brittle layers of laminated glass. Int J Impact Eng 2014;69:80–5.
[18] Przewłócki J, Zielińska M, Grębowski K. Numerical Modelling of Connections Between Stones in Foundations of Historical Buildings. IOP Conference Series: Earth and Environmental Science 2017;95:1–8.
[19] Du Bois P, Kolling S, Fassnacht W. Modelling of safety glass for crash simulation. Comput Mater Sci 2003;28:675–83.
[20] Zielińska M, Rucka M. Imaging of Increasing Damage in Steel Plates Using Lamb Waves and Ultrasound Computed Tomography. Materials 2021;14:5114.
[21] Timmel M, Kolling S, Osterrieder P, Du Bois P. A finite element model for impact simulation with laminated glass. Int J Impact Eng 2007;34:1465–78.
[22] Hidallana-Gamage HD, Thambiratnam DP, Perera NJ. Failure analysis of laminated glass panels subjected to blast loads. Eng Fail Anal 2014;36:14–29.
[23] Xihong Z, Hong H, Guowei M. Parametric study of laminated glass window response to blast loads. Eng Struct 2013;56:1707–17.
[24] Peng Y, Yang J, Deck C, Willinger R. Finite element modeling of crash test behavior for windshield laminated glass. Int J Impact Eng 2013;57:27–35.
[25] Zhang X, Hao H, Ma G. Laboratory test and numerical simulation of laminated glass window vulnerability to debris impact. Int J Impact Eng 2013;55:49–62.
[26] Zhang X, Hao H, Ma G. Parametric study of laminated glass window response to blast loads. Eng Struct 2013;56:1707–17.
[27] Centelles X, Ramon J, Castro L, Cabeza F. Experimental results of mechanical, adhesive, and laminated connections for laminated glass elements – A review. Eng Struct 2019;180:192–204.
[28] Xu J, Li Y. Study of damage in windshield glazing subject to impact by a pedestrian's head. Proc Inst Mech Eng Part D: J Automobile Eng 2009;223:77–84.
[29] Grębowski K, Rucka M, Wilde K. Non-Destructive Testing of a Sport Tribune under Synchronized Crowd-Induced Excitation Using Vibration Analysis. Materials 2019;12:1–19.
[30] Xu W, Zang M. Four-point combined DE/FE algorithm for brittle fracture analysis of laminated glass. Int J Solids Struct 2014;51:1890–900.
[31] Taraszkiewicz A, Grębowski K, Taraszkiewicz K, Przewłócki J. Contemporary Architectural Design in the Context of Historic Remains: The Case of the Old City of Gdańsk. Heritage and Society 2022;1:1–19.
[32] Gao W, Zang M. The simulation of laminated glass beam impact problem by developing fracture model of spherical DEM. Eng Anal Boundary Elem 2014;42:2–7.
[33] Xu J, Li Y, Chen X, Yan Y, Ge D, Zhu M, et al. Characteristics of windshield cracking upon low-speed impact: numerical simulation based on the extended finite element method. Comput Mater Sci 2010;48:582–8.
[34] Chen S, Zang M, Xu W. A three-dimensional computational framework for impact fracture analysis of automotive laminated glass. Comput Methods Appl Mech Eng 2015;294:72–99.
[35] Xihong Z, Hong H. Experimental and numerical study of boundary and anchorage effect on laminated glass windows under blast loading. Eng Struct 2015;90:96–116.
[36] Aiello S, Campione G, Minafò G, Scibilia N. Compressive behaviour of laminated structural glass members. Eng Struct 2011;33:3402–8.
[37] Lopez-Aenlle M, Pelayo F. Dynamic effective thickness in laminated-glass beams and plates. Compos B Eng 2014;67:332–47.
[38] Galuppia L, Royer-Carfagniab G. Enhanced Effective Thickness for laminated glass beams and plates under torsion. Eng Struct 2020;206:110077.
[39] Chen H, Lei Z, Zang M. LC-Grid: a linear global contact search algorithm for finite element analysis. Comput Mech 2014;54:1285–301.
[40] Wang SP, Nakamachi E. The inside–outside contact search algorithm for finite element analysis. Int J Numer Methods Eng 1997;40:3665–85.
[41] Biolzi L, Simoncelli M. Overall response of 2-ply laminated glass plates under out-of-plane loading. Eng Struct 2022;256:113967.
[42] Livermore Software Technology 2022.
[43] Jagota A, Bennison S, Smith C. Analysis of a compressive shear test for adhesion between elastomeric polymers and rigid substrates. Int J Fract 2000;104:105–30.
[44] Galuppi L, Royer-Carfagni G. A homogenized model for the post-breakage tensile behavior of laminated glass. Compos Struct 2016;154:600–15. https://doi.org/10.1016/j.compstruct.2016.07.052.
[45] Muralidhar S, Jagota A, Bennison SJ, Saigal S. Mechanical behaviour in tension of cracked glass bridged by an elastomeric ligament. Acta Mater 2000;4:4577–88. https://doi.org/10.1016/S1359-6454(00)00244-5.
[46] Galuppi L, Royer-Carfagni G. The post-breakage response of laminated heat-treated glass under in plane and out of plane loading. Compos B Eng 2018;147:227–39. https://doi.org/10.1016/j.compositesb.2018.04.005.
[47] Ivanov IV, Velchev DS, Georgiev NG, Ivanov ID, Sadowski T. A plate finite element for modelling of riplex laminated glass and comparison with other computational models. Meccanica 2016;51:341–58.
[48] Baraldi D, Cecchi A, Foraboschi P. Broken tempered laminated glass: Non-linear discrete element modeling. Compos Struct 2016;140:278–95. https://doi.org/10.1016/j.compstruct.2015.12.050.
[49] Freddi F, Mingazzi L. Phase Field Simulation of Laminated Glass Beam. Materials 2020;13(14):3218. https://doi.org/10.3390/ma13143218.
[50] Galuppi L, Royer-Carfagni G. Laminated beams with viscoelastic interlayer. Int J Solids Struct 2012;49:2637–45. https://doi.org/10.1016/j.ijsolstr.2012.05.028.
[51] Pelayo F, Lamela-Rey MJ, Muniz-Calvente M, López-Aenlle M, Álvarez-Vázquez A, Fernández-Canteli A. Study of the time-temperature-dependent behaviour of PVB: Application to laminated glass elements. Thin-Walled Struct 2017;119:324–31. https://doi.org/10.1016/j.tws.2017.06.030.
[52] Di Paolaa M, Galuppi L, Royer CG. Fractional viscoelastic characterization of laminated glass beams under time-varying loading. Int J Mech Sci 2021;196:106274. https://doi.org/10.1016/j.ijmecsci.2021.106274.
[53] Viviani L, Di Paola M, Royer-Carfagni G. Fractional viscoelastic modeling of laminated glass beams in the pre-crack state under explosive loads. Int J Solids Struct 2022;248:111617. https://doi.org/10.1016/j.ijsolstr.2022.111617.
[54] Amadio C, Bedon C. Viscoelastic spider connectors for the mitigation of cable-supported façades subjected to air blast loading. Eng Struct 2012;42:190–200. https://doi.org/10.1016/j.engstruct.2012.04.023.
[55] Viviani L, Royer-Carfagni G. How dissipative devices could enhance the capacity of glazed surfaces under impacting blast waves. Int J Non Linear Mech 2021;137:103813. https://doi.org/10.1016/j.ijnonlinmec.2021.103813.
[56] Arrigoni M, Bedon C, van Doormaal JCAM, Haberacker C, Hüsken G, Millon O, et al. Design of Blast-Loaded Glazing Windows and Facades: A Review of Essential Requirements towards Standardization. Advances in Civil Engineering 2016;2016:1–15. https://doi.org/10.1155/2016/2604232.
[57] CEN / TS 19100: 2021 "Design of glass structures".
[58] Geiler G, Netzker C, Kaliske M. Discrete crack path prediction by an adaptive cohesive crack model. EngFractMech 2010;77:3541–57.
[59] Siromani D, Awerbuch J, Tan TM. Finite element modeling of the crushing behavior of thin-walled cfrp tubes under axial compression. Compos Part B: Eng 2014;64:50–8.
[60] Soutis C, Mohamed G, Hodzic A. Modelling the structural response of glare panels to blast load. Compos Struct 2011;94:267–76.
[61] Van den Bosch M, Schreurs P, Geers M. An improved description of the exponential Xu and Needleman cohesive zone law for mixed-mode decohesion. EngFractMech 2006;73:1220–34.
[62] Liu B, Xu T, Xu X, Wang Y, Sun Y, Li Y. Energy absorption mechanism of polyvinyl butyral laminated windshield subjected to head impact: experiment and numerical simulations. Int J Impact Eng 2016;90:26–36. https://doi.org/10.1016/j.ijimpeng.2015.11.010.
[63] Xu J, Li Y, Ge D, Liu B, Zhu M. Experimental investigation on constitutive behavior of PVB under impact loading. Int J Impact Eng 2011; 38: 106–14. http://dx.10.1016/j.ijimpeng.2010.10.001.
[64] Reddy JN. Mechanics of laminated composite plates and shells theory and analysis. Boca Raton: CRC Press; 2004.
[65] Chen J, Xu J, Yao X, Liu B, Xu X, Zhang Y, et al. Experimental investigation on the radial and circular crack propagation of PVB laminated glass subject to dynamic out-of-plane loading. Eng Fract Mech 2013;112–113:26–40. https://doi.org/10.1016/j.engfracmech.2013.09.010.
[66] Pyttel T, Liebertz H, Cai J. Failure criterion for laminated glass under impact loading and its application in finite element simulation. Int J Impact Eng 2011;38:252–63. https://doi.org/10.1016/j.ijimpeng.2010.10.035.
[67] Voyiadjis GZ, Rashid K, Al-Rub A. Non-local coupling of viscoplasticity and anisotropic viscodamage for impact problems using the gradient theory. Archives of Mechanics 2014;55(1):39–89.
[68] Lu J, Papadopoulos P. A covariant constitutive description of anisotropic non-linear elasticity. Zeitschrift für angewandte Mathematik und Physik ZAMP 2000;51:204–17. https://doi.org/10.1007/s000330050195.
[69] Sumelka W, Nowak M, Nassr AA, Al-Rifaie H, Malendowski M, Gajewski T, et al. Int J Impact Eng 2021;158:104024. https://doi.org/10.1016/j.ijimpeng.2021.104024.
[70] Safaei M, Lee M-G, Zang S-I, De Waele W. An evolutionary anisotropic model for sheet metals based on non-associated flow rule approach. Comput Mater Sci 2014;81:15–29. https://doi.org/10.1016/j.commatsci.2013.05.035.
[71] Manzari MT, Yonten K. On implementation and performance of an anisotropic constitutive model for clays. Int J Comput Methods 2014;11(2):1342009. https://doi.org/10.1142/S0219876213420097.